



HAL
open science

Astronomical calibration of the OAE1b from the Col de Pré-Guittard section (Aptian–Albian), Vocontian Basin, France

Fatima-Zahra Ait-Itto, Mathieu Martinez, Jean-François Deconinck, Stéphane Bodin

► To cite this version:

Fatima-Zahra Ait-Itto, Mathieu Martinez, Jean-François Deconinck, Stéphane Bodin. Astronomical calibration of the OAE1b from the Col de Pré-Guittard section (Aptian–Albian), Vocontian Basin, France. *Cretaceous Research*, 2023, 150, pp.105618. 10.1016/j.cretres.2023.105618 . insu-04128080

HAL Id: insu-04128080

<https://insu.hal.science/insu-04128080>

Submitted on 14 Jun 2023

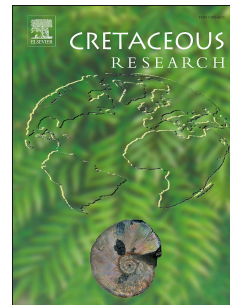
HAL is a multi-disciplinary open access archive for the deposit and dissemination of scientific research documents, whether they are published or not. The documents may come from teaching and research institutions in France or abroad, or from public or private research centers.

L'archive ouverte pluridisciplinaire **HAL**, est destinée au dépôt et à la diffusion de documents scientifiques de niveau recherche, publiés ou non, émanant des établissements d'enseignement et de recherche français ou étrangers, des laboratoires publics ou privés.

Journal Pre-proof

Astronomical calibration of the OAE1b from the Col de Pré-Guittard section (Aptian–Albian), Vocontian Basin, France

Fatima-Zahra Ait-Itto, Mathieu Martinez, Jean-François Deconinck, Stéphane Bodin



PII: S0195-6671(23)00146-5

DOI: <https://doi.org/10.1016/j.cretres.2023.105618>

Reference: YCRES 105618

To appear in: *Cretaceous Research*

Received Date: 16 December 2022

Revised Date: 25 May 2023

Accepted Date: 5 June 2023

Please cite this article as: Ait-Itto, F.-Z., Martinez, M., Deconinck, J.-F., Bodin, S., Astronomical calibration of the OAE1b from the Col de Pré-Guittard section (Aptian–Albian), Vocontian Basin, France, *Cretaceous Research*, <https://doi.org/10.1016/j.cretres.2023.105618>.

This is a PDF file of an article that has undergone enhancements after acceptance, such as the addition of a cover page and metadata, and formatting for readability, but it is not yet the definitive version of record. This version will undergo additional copyediting, typesetting and review before it is published in its final form, but we are providing this version to give early visibility of the article. Please note that, during the production process, errors may be discovered which could affect the content, and all legal disclaimers that apply to the journal pertain.

© 2023 Elsevier Ltd. All rights reserved.

Ait-Itto Fatima-Zahra: I participated in the field trip, collecting and analyzing samples, and taking the lead in writing the original draft manuscript.

Mathieu Martinez: Significant contributions to the conceptualization and investigation of this work, which greatly contributed to the improvement of the manuscript. He's suggestions and inputs played a vital role in shaping the overall direction of the research.

Jean-François Deconinck: Participation in the field and sample collection with strong implication in the preparation and analysis of samples for $\delta^{13}\text{C}_{\text{org}}$ measurement was crucial to obtaining reliable data. Additionally, he made valuable contributions to manuscript correction and provided insightful recommendations, enhancing the quality of the final publication.

Stéphane Bodin: Contribution to the fieldwork, including sample collection and organic matter analysis (TOC/ HI/ OI) with significant contribution in the amelioration of the quality of the manuscript.

The collaborative efforts of all the co-authors were integral to the successful completion of this research. Their individual contributions, ranging from fieldwork to data analysis and manuscript improvement, have enriched the study's findings and its overall scientific value.

1 **Astronomical calibration of the OAE1b from the Col de**
2 **Pré-Guittard section (Aptian–Albian), Vocontian Basin,**
3 **France**

4 Fatima-Zahra Ait-Itto ^{a&b}, Mathieu Martinez ^a, Jean-François Deconinck ^c, Stéphane Bodin ^d

5 a Univ Rennes, CNRS, Géosciences Rennes – UMR 6118, 35000 Rennes, France

6 b Univ Rennes, CNRS, Institut des Sciences Chimiques de Rennes, 35042 Rennes, France

7 c Biogéosciences, UMR 6282, CNRS, Université Bourgogne Franche-Comté, 6 Boulevard Gabriel, 21000, Dijon, France

8 d Department for Geoscience, Aarhus University, Hoegh-Guldbergs Gade 2, 8000 Aarhus C, Denmark

9
10 **Abstract**

11 A high-resolution spectral analysis was performed on magnetic susceptibility (MS) in the Col
12 de Pré-Guittard section (CPG), Vocontian Basin, France to provide a new astronomical time
13 scale of the Aptian-Albian transition and to explore the link between Milankovitch cycles and
14 the occurrence of four laminated black shales events, namely Jacob, Kilian, Paquier and
15 Leenhardt constituting the OAE 1b. The spectral analysis performed on the CPG section records
16 the imprint of a strong predominance of the precession, and 100-kyr and 405-kyr eccentricity
17 cycles. Based on the number of 405-kyr eccentricity cycles, the duration of the interval
18 encompassing the Jacob to Leenhardt levels is calculated at 4.03 myr. The duration between
19 Jacob, Kilian, Paquier and Leenhardt Events are respectively calculated at 1.55 myr, 1.62 myr,
20 and 0.93 myr. The duration calculated for the occurrence of these events is not related to the
21 Milankovitch cycles. However, these events are recorded near local maxima of the 405-kyr
22 filter. Our results show that the 405-kyr eccentricity impacted the recurrence of anoxic levels
23 in the Vocontian Basin, although additional factors, such as the emplacement of flood basalts
24 or oceanic basaltic plateaus have contributed to the development of larger scale marine anoxia.

25 **Keywords:** Aptian – Albian, Cyclostratigraphy, Magnetic Susceptibility, OAE1b, Vocontian
26 Basin

27 **1. Introduction**

28 The Aptian-Albian transition (~113 Ma) is punctuated by a series of widespread black shale
29 deposits, collectively known as OAE1b. Four levels are frequently mentioned from the oldest
30 to the youngest: Jacob, Kilian, Paquier, and Leenhardt levels (Br  h  ret, 1985, 1988, 1997;
31 Kennedy et al., 2000; F  llmi, 2012; Coccioni et al., 2014; Herrle et al., 2015; Matsumoto et al.,
32 2020; Leandro et al., 2022). The Aptian-Albian boundary is located at the first occurrence of
33 the planktonic foraminifer *Microhedbergella renilaevis*, within the Kilian Level (Kennedy et
34 al., 2017) and the OAE 1b interval started at a time of decreasing temperatures, which reached
35 a minimum near the Jacob or in between the Jacob and Kilian levels before increasing through
36 the early Albian (McAnena et al., 2013; Bodin et al., 2015; Bottini et al., 2015; Bottini and
37 Erba, 2018). This minimum in temperatures is described as the Aptian-Albian boundary cold
38 snap (Mutterlose et al., 2009) and likely led to the development of polar ice (Price, 1999;
39 Rodr  guez-L  pez et al., 2016). Within this broad trend, the anoxic levels corresponded to warm
40 pulses (Wagner et al., 2008; Bottini and Erba, 2018), accompanied by rapid sea-level rise
41 phases, increased weathering conditions, and detrital supply (Mill  n et al., 2014; Benamara et
42 al., 2020) and decreased sea-surface salinity (Wagner et al., 2008). In pelagic environments, the
43 anoxic layers marked a decrease in benthic foraminifera diversity and abundance, while
44 opportunistic species prevailed (Erbacher et al., 1999; Friedrich, 2010). Species turnover and
45 change in morphology occurred among the planktic foraminifera, likely in response to these
46 paleoceanographic changes (Huber and Leckie, 2011). Radiolaria also experienced stepwise
47 extinctions around the Aptian-Albian boundary (Erbacher and Thurow, 1997).

48 Questions arose on the forcing factor of these recurrent short-lived anoxic events. A negative
49 Os-isotope excursion has been found in the Kilian Level in the Umbria-Marche Basin, that

50 correlate with the planktonic foraminiferal turnover suggesting a multiple submarine volcanic
51 events (central Italy; Matsumoto et al., 2020). The link was confirmed by significant
52 enrichments in Hg in DSDP Site 545, offshore Morocco, Eastern North Atlantic (Bracquat et
53 al., 2022) suggest a link with the activity of the Kerguelen Plateau. Conversely, no evidence of
54 volcanic activity has been found in the Paquier Level (Benamara et al., 2020; Matsumoto et al.,
55 2020). According to the last Geologic Time Scale 2020, the duration between the OAE 1b
56 events are; *ca.* 1.3 myr from the Jacob to the Kilian levels, *ca.* 1.9 myr from the Kilian to the
57 Paquier levels and *ca.* 1 myr from the Paquier to the Leenhardt levels (Gale et al., 2020). These
58 durations are close to the periods of the long obliquity cycle (1.2 myr) and long eccentricity
59 cycle (2.4 myr) (Laskar et al., 2004), which questions the role of these long orbital cycles on
60 the recurrence of anoxia around the Aptian-Albian transition (Wang et al., 2022). However, the
61 durations estimated between the anoxic levels have demonstrated to be unstable from geologic
62 time scale to another, which prevents from determining the forcing factors at the onset of these
63 events.

64 Here, we perform spectral analyses on magnetic susceptibility signal acquired at very high-
65 resolution in the Col de Pré-Guittard reference section (Albian GSSP, Vocontian Basin, SE
66 France), in which these four well-exposed anoxic events have been defined (Bréhéret, 1997;
67 Kennedy et al., 2017) to propose a new astronomical calibration of the Aptian-Albian transition
68 and test the role of the orbital forcing on the inception of these anoxic events.

69

70 2. Geological setting

71 The Vocontian Basin (SE France) was located at a paleolatitude of 25-30 °N and corresponded
72 to a paleo-passive margin between the NW part of the Alpine Tethys Ocean and the Atlantic
73 Rift (Dercourt et al., 1993) surrounded by slopes and platforms (Fig. 1A, B). In the latest
74 Hauterivian – early Aptian the basin was surrounded by the Urgonian carbonate platforms
75 including the Provence platform to the South, the Ardèche-Vivarais platform to the West and
76 Chartreuse-Vercors (Dauphiné platform) to the North. The Urgonian carbonate platform was
77 drowned in the early Aptian and never recovered (Arnaud et al., 2017). After this event, during
78 the Aptian-Albian, the Vocontian Basin was characterized by the deposition of the “Marnes
79 Bleues” (Blue Marls) Formation, an hemipelagic marl-dominated sedimentation regime
80 characterized by terrigenous fluxes comprising quartz and various clay minerals dominated by
81 illite, smectite and kaolinite (Ghirardi et al., 2014, Coentini et al., 2020) mixed with biogenic
82 components dominated by nanofossils and foraminifers. The paleo-water depth of the
83 Vocontian Basin is estimated to have been several hundred meters based on palynological
84 investigations (Wilpshaar and Leerveld, 1994). The Aptian-Albian transition is mainly
85 composed by a monotonous succession of marly hemipelagic deposits intercalated by rare
86 limestone layers and recurrent black shale levels (Bréhéret, 1997), some of these being
87 prominent in the landscape in the Vocontian series and correlated at a supra regional scale
88 (Jacob, Kilian, Paquier, Leenhardt). Slumps, turbidites and occasional diagenetic barite
89 concretion accumulations are also observed (Bréhéret and Brumsack, 2000).

90

91 2.1 Studied section

92 The Col de Pré-Guittard outcrop is located in the northwestern part of the Vocontian Basin, SE
93 France, near the village of Arnayon in the *Département de la Drôme* (F-26470), *ca.* 11 km
94 northwest of Rémuzat and 2 km from la Motte-Chalançon (Fig. 2A). The section is well
95 exposed over hundreds of meters. The lithological succession has been described in detail by
96 Bréhéret (1997). It is characterized by monotonous sequences of marly hemipelagic to pelagic
97 deposits of the Marnes Bleues Formation, in which intercalate limestone and black shale levels
98 (Fig. 1C, D), among which are the Jacob, Kilian, Paquier and Leenhardt have been identified
99 as prominent levels correlated beyond the Vocontian Basin. The Col de Pré-Guittard section is
100 well studied, notably because it hosts the GSSP of the Aptian-Albian boundary (Kennedy et al.,
101 2017). The Col de Pré-Guittard section has been chosen for our purpose considering both the
102 detailed biostratigraphy and the lithology consisting mainly of monotonous hemipelagic marls
103 with rare syn-sedimentary slumping, which are otherwise frequent in the Vocontian Basin
104 (Friès and Parize 2003). The biostratigraphic divisions were established by ammonites
105 (*Hypacanthoplites jacobi*, *Leymeriella germanica*, and *Leymeriella tardefurcata* Ammonite
106 Zone), planktonic foraminifera, and calcareous nannofossils (Kennedy et al., 2000; Herrle et
107 al., 2003). The studied section has been measured from the upper part of the Fromaget
108 calcareous bundle (uppermost Aptian) to *ca.* 10 m above the Leenhardt horizon. It covers the
109 four main black levels of the OAE 1b (Jacob, Kilian, Paquier, and Leenhardt).

110 2.2. Location of the GSSP section compared to Kennedy et al. (2017)

111 In the formal proposal of the GSSP of the Albian stage (Kennedy et al., 2017), the location of
112 the GSSP section in their Figure 2 does not correspond to the picture shown in their Figure 3.
113 After discussions, it appeared that it misled several teams working in the area, so we aim here
114 at clarifying the location of the sections. The photograph picture of the section shown in Figure

115 3 of Kennedy et al. (2017) is actually located 1.38 km further NW (44°30'28" N, 5°17'50"E).
116 In our Figure 2A, it is labelled as "CPG-1 – GSSP". This section extends from the Jacob Event
117 to the Kilian Event. In this section, the Kilian Level was labelled in the photograph picture in
118 Kennedy et al. (2017) and perfectly observed as a prominent black shale layer. The Jacob Level
119 corresponds to a black shale layer outcropping 1.5 m above a bundle of prominent limestone
120 beds called "Fromaget bundle", also labelled in the photograph picture in Kennedy et al. (2017).
121 The section indicated as the GSSP in Figure 2 of Kennedy et al. (2017) is referred in our Figure
122 2B as "CPG-2" and extends from the Kilian Event to the Middle Albian. The Paquier Level is
123 visible in the landscape as a prominent black shale horizon, as documented in the photograph
124 picture in Figure 8 of Corentin et al. (2020). The Kilian and Leenhardt levels did not appear as
125 prominent after a first investigation of the series, so we undertook 280 analyses of $\delta^{13}\text{C}_{\text{org}}$
126 measurements and 113 organic matter analyses to locate the Kilian and Leenhardt levels. Both
127 the Kilian and the Leenhardt should appear with higher TOC and drastic increase Hydrogen
128 Index (HI) in the organic-matter analysis. The Kilian Level should in addition be documented
129 by a negative excursion both in $\delta^{13}\text{C}_{\text{carb}}$ and $\delta^{13}\text{C}_{\text{org}}$ (Herrle et al., 2004; Bodin et al., 2023). The
130 samples were selected after performing the astrochronology of the section, so that there is at
131 least a sample per precession cycle (~20 kyr). The intervals where we suspected the presence
132 of the Kilian and the Leenhardt Levels were more densely covered. The intervals analyzed for
133 spectral analyses are not affected by slumps. A decimetric glauconitic sandstone layer
134 nonetheless outcrops at level 33.7 m in CPG-2. The durations calculated will be based on the
135 longest cycles to limit the probability of missed cycles and the durations thereafter are described
136 as minimum durations.

137

138 **3. Material and methods**

139 **3.1. Field sampling**

140 A total of 3249 samples were collected with a high-resolution stratigraphic step of 0.05 m
141 recovering the four black levels (Jacob, Kilian, Paquier, and Leenhardt). The sample distance
142 was selected to preserve the quality of the high frequencies. The measurements have been
143 undertaken using a Jacob stick to limit the errors in the sample position. The weathered surface
144 was removed and the samples were cleaned. The samples were crushed using a clean hammer
145 and then weighted for magnetic susceptibility measurements. For chemical analysis, the
146 samples were powdered using an agate mortar.

147 **3.2. Magnetic susceptibility**

148 The magnetic susceptibility (MS) measurement was conducted with Agico KLY-3 at the
149 University of Rennes, in a total of 3249 samples were measured. The weighted samples are
150 placed in a small plastic bag and introduced manually inside to the instrument. Before each
151 series of measurements, an empty bag is measured for the blank correction and normalized to
152 sample mass. The mass-specific MS is reported in m^3/kg .

153 **3.3. Spectral analyses**

154 Prior to the spectral analyses, the long-term evolutions of the magnetic susceptibility were
155 calculated and subtracted using LOWESS method (LOcally WEighted Scatterplot Smoothing;
156 Cleveland, 1979) to ensure the stationarity of the signal. Then, a multi-taper spectral analysis
157 was performed using three 2π prolate tapers (2π -MTM spectrum; Thomson, 1982, 1990). The
158 confidence levels against a red-noise were calculated using the robust procedure of Mann and
159 Lees (1996). It consists in calculating the moving median over 20 % of the spectrum and fitting
160 a red-noise model on this moving median. The confidence levels are then extrapolated assuming
161 a χ^2 distribution. The spectral peaks exceeding the 95 % confidence levels are decreased to their

162 adjacent spectral power and the procedure is iterated another time. This procedure allows the
163 spectral peaks not to be counted in the background estimation). Then a time-frequency weighted
164 Fast Fourier transform (TF-WFFT; Martinez et al., 2015) was performed to trace the evolution
165 of the periods along the sedimentary series. A correlation coefficient (COCO) was also applied
166 to quantify which sedimentary rate leads to the best correlation between the spectrum of the
167 sedimentary series and the spectrum of the orbital periods (Li et al., 2019). In this study 10.000
168 Monte Carlo simulations were applied to ensure stability of the results and reproducibility.
169 Evolutive COCO (eCOCO) were also applied on each series. The size of the window was
170 adapted to each series, depending on the estimated most likely sedimentation rates from COCO.
171 Each interpreted signal as orbital forcing is isolated and filtered using Taner lowpass and
172 bandpass filters (Prokopenko et al., 2006). The sedimentary cycles were then anchored to their
173 corresponding orbital periods, allowing depth-time conversions to be done. The orbital
174 procedure used here assumes a constant duration of 405 kyr between two repetitions of the filter
175 of the 405-kyr eccentricity cycle and a constant sedimentation rate between two consecutive
176 anchor points. To precisely locate the black levels in the CPG-2, 290 samples were selected
177 according to a precession 20-kyr filter to be analyzed on carbonate content, Total Organic
178 Carbon (TOC), and carbon isotope on organic matter ($\delta^{13}\text{C}_{\text{org}}$).

179 **3.4. Carbonate content and carbon isotope**

180 The calcium carbonate content and $\delta^{13}\text{C}_{\text{org}}$ were measured on 280 powdered samples at
181 Biogéosciences laboratory, Université de Bourgogne/Franche-Comté in Dijon, France. The
182 $\delta^{13}\text{C}_{\text{org}}$ was measured on carbonate-free residues. Sample powders were reacted with HCl (2 N)
183 at room temperature for 2 h to remove carbonate phases. Residues were rinsed with deionized
184 distilled water until neutral, centrifuged (4500 rpm for 15 min), and dried at 50 °C overnight.
185 Aliquots of dried decarbonated samples (~ 7–50 mg) were then weighed in tin capsules. The
186 $\delta^{13}\text{C}_{\text{org}}$ measurements were performed on a Vario MICRO cube elemental analyzer (Elementar,

187 Hanau, Germany) coupled in continuous flow mode to an IsoPrime stable isotope ratio mass
188 spectrometer (Isoprime, Manchester, UK). USGS40 L-Glutamic acid (C = 40.8 wt%;
189 $\delta^{13}\text{C}_{\text{VPDB}} = -26.39 \pm 0.04 \text{ ‰}$) and IAEA-600 Caffeine ($\delta^{13}\text{C}_{\text{VPDB}} = -27.77 \pm 0.04 \text{ ‰}$) certified
190 reference materials were used for calibration. The carbon isotopic composition is expressed in
191 delta notation and reported in per mil (‰) relative to the Vienna Pee Dee Belemnite (V-PDB)
192 standard; external reproducibility based on duplicate analyses of samples is better than $\pm 0.2 \text{ ‰}$
193 (1σ).

194 **3.5. Total organic carbon (TOC)**

195 The organic matter characterization was performed on samples from the CPG-2 section using
196 the Hawk (Wildcat Technology) anhydrous pyrolysis carbon analysis system at the
197 Lithospheric Organic Carbon (LOC) lab, Department of Geoscience, Aarhus University,
198 Denmark. A total of 113 samples were measured and calibrated using IFP 160000 standard.
199 Precision and accuracy of measurements were better than 5 %. Four parameters are considered
200 here: total organic carbon (TOC, wt%), oxygen index (OI, mg CO₂/g TOC), Hydrogen index
201 ((HI, mg HC/ g TOC, HC = hydrocarbons), and Tmax(°C).

202 **4. Results**

203 **4.1. Magnetic susceptibility**

204 In Col de Pre Guittard section 1 (CPG-1), the mass-specific magnetic susceptibility (MS) ranges
205 from $3.05 \times 10^{-8} \text{ m}^3/\text{kg}$ to $6.66 \times 10^{-8} \text{ m}^3/\text{kg}$ (Fig. 3). The MS series has an average value of
206 $5.27 \times 10^{-8} \text{ m}^3/\text{kg}$. The long-term trend of the MS signal (red curve) shows a low average value
207 around $4.94 \times 10^{-8} \text{ m}^3/\text{kg}$ in the first 23 m of the section, which corresponds to the most
208 carbonated interval. Then, from level 23 m to 38 m, the trend shows a higher value reaching an
209 average nearby to $5.65 \times 10^{-8} \text{ m}^3/\text{kg}$, which corresponds to an increase in detrital component
210 (Fig. 3A). After the short period of decreasing average MS values, from level 38 m to 48 m, the

211 trend in the MS values increases again from the Kilian Level to the top of CPG-1 to reach
212 $5.60 \times 10^{-8} \text{ m}^3/\text{kg}$.

213 In Col de Pré-Guittard section 2 (CPG-2), the mass-specific MS series range from 7.57×10^{-9}
214 m^3/kg to $6.44 \times 10^{-8} \text{ m}^3/\text{kg}$ with an average value of $4.34 \times 10^{-8} \text{ m}^3/\text{kg}$. The long-term trend of
215 the MS series (red curve) shows that the values decrease in the first 45 m. Then the values
216 stabilized around level 45 m to the top of the section (Fig. 3B). In this interval, the CaCO_3
217 content has an average value of 47 % (measured on 290 samples). The MS and CaCO_3 are
218 inversely correlated $r = -0.63$. Knowing that the Blue Marls are dominantly composed of clay
219 minerals and CaCO_3 , this suggests that the paramagnetic clay minerals (illite and smectite)
220 control the SM signal (Fig. 4). This result was expected since previous works in the same
221 formation highlighted this inverse correlation (Ghirardi et al., 2014).

222 **4.2. Organic carbon isotope and pyrolysis analysis**

223 The $\delta^{13}\text{C}_{\text{org}}$ values measured at CPG-2 range from -27.69 ‰ VPDB to -23.85 ‰ VPDB , with
224 an average value of -25.88 ‰ VPDB (Fig. 3F). The $\delta^{13}\text{C}_{\text{org}}$ values show a broad increase from
225 -26.5 ‰ VPDB at the base of CPG-2 to -25 ‰ VPDB at level 30 m. Then the values are stable
226 at around -26 ‰ VPDB with higher-frequency fluctuations from level 30 m to the top of the
227 section. The lowest $\delta^{13}\text{C}_{\text{org}}$ values drop to -27.69 ‰ and are observed at the base of CPG-2,
228 together with HI values higher than 180 mgHC/gTOC) and TOC values higher than 2 % (Fig.
229 5A, B and C). These features perfectly align with the organic geochemical signature of the
230 Kilian Level at Les Briers section (Fig. 5D, E and F), eastern Vocontian Basin (Bodin et al.
231 2023). According to these, the identification of Kilian level can be confidently proposed at the
232 base of the section CPG-2.

233 The Kilian Level thus records the most negative value of the section with values around -27.69
234 ‰ followed by increasing values reaching -23.85 ‰ at 5 m. At 8.4 m, a prominent negative

235 excursion is recorded with values decreasing to -27.42 ‰, likely corresponding to the Horizon
236 Noir (HN1; Br  h  ret, 1997), one of the dark horizons identified in the Vocontian Basin. In the
237 Paquier Level, the $\delta^{13}\text{C}_{\text{org}}$ registered a value around -26 ‰ at 53 m. Then, in the upper part of
238 the section, a distinct negative value of -27.08 ‰ VPDB is recorded, corresponding to the
239 Leenhardt Level. The Total Organic Carbon (TOC) contents at CPG-2 range from 0.53 wt% to
240 2.66 wt% (Fig. 3C) with an average value of 0.76 wt%. The long-term trend shows in general
241 values lower than 1 % with a significant increase in the values corresponding to the black level
242 reaching a maximum of 2.66 wt% in the Kilian Level. Furthermore, the Paquier and Leenhardt
243 levels record a small increase in TOC values reaching around 1.15 wt%. for both levels. The
244 Highest Hydrogen Index (HI) values are registered respectively at the Kilian (188
245 mgHC/gTOC), Paquier, (88 mgHC/gTOC) and Leenhardt (163 mgHC/gTOC) (Fig. 3D). The
246 rest of the samples register values less than 50 mgHC/gTOC. The Oxygen Index (OI) values
247 range from 20 to 114 mgCO₂/gTOC with an average of 40.50 mgCO₂/gTOC; (Fig. 3E).
248 Significant increase on TOC and HI below the Paquier Level, at 49 m, corresponds to HN8
249 (Br  h  ret, 1997).

250 4.3 Spectral analyses

251 4.3.1 CPG-1

252 The spectral analysis performed on the MS series in Col de Pr  -Guittard section (CPG-1) shows
253 the presence of significant periods with confidence level higher than 99 % at 10 m, 3.6 m, 1.8
254 m, 1.5 m, 0.66 m, 0.54 m and 0.48 m (Fig. 6A). A spectrogram was performed on 25-m width
255 windows focusing on the lowest frequencies (Fig. 7C). Another spectrogram was performed on
256 10-m width windows after filtering the lowest frequencies with a Taner low-pass filter in order
257 to focus on the high frequencies (frequency cut: 0.2171 cycles/m, Fig. 7D). CPG-1 first interval,
258 from levels 0 m to 25 m, shows the predominance of two bands at 12 m and 0.65 m (Figs. 7C,
259 7D). Another band is observed with high amplitudes from 10 to ~30 m at 3.4 m (Figs. 7C, 7D).

260 A last band is observed with lower amplitudes around 1.5 m at level 6 m. The second interval,
261 from level 25 m to the top of CPG-1, shows the presence of a band at 8.6 to 8.7 m with low
262 amplitudes up to 43 m and then with high amplitudes (Fig. 7C). Two other group of periods are
263 recorded from 1.6 to 2.7 m and from 0.47 m to 0.45 m (Fig. 7D). Two periods at 0.95 and 0.71
264 m appear punctually, respectively at level 30 m and at the top of the series.

265 The COCO method applied to the CPG-1 show the highest significant correlation at (p -value
266 $<1 \times 10^{-3}$) at sedimentation rates around 0.8 cm/kyr, 1.7 cm/kyr, 2.7 cm/kyr, and 3.5 cm/kyr (Fig.
267 6B). The eCOCO procedure applied on 25-m width windows show a significant correlation at
268 sedimentation rates around 3.5 cm/kyr and 2.5 cm/kyr from level 0 m to level 25 m then the
269 sedimentation rate decreases to reach 1.9 cm/kyr from level 25 m to the top of the section. (Fig.
270 7E). According to the spectral analysis, the section can be subdivided in two intervals to limit
271 the effect of the sedimentation: Interval 1 from level 0 m to 30 m, in which the sedimentation
272 rate is around 3 cm/kyr, and interval 2 from 25 m to the top of the section, in which the
273 sedimentation rate is around 2 cm/kyr. We left 5 m of recovery between intervals 1 and 2 to
274 ensure continuity of the filters (Fig. 7B).

275 The 2π -MTM spectrum performed on Interval 1 of CPG-1 (from level 0 m to 30 m) shows the
276 presence of significant spectral peaks at 14 m, 3.4 m, and from 0.72 m to 0.43 m exceeding the
277 99 % confidence level (Fig. 6C). The COCO analysis recorded shows a highly significant
278 correlation (p -value $<1 \times 10^{-3}$) at sedimentation rates at 3.5 cm/kyr additional correlation is
279 registered around 2.7 cm/kyr (Fig. 6D). The 2π -MTM spectrum performed on Interval 2 of
280 CPG-1, from level 25 m to the top of the section, shows the presence of a significant peak at
281 the 2π -MTM spectrum with a confidence level higher than 99% at 8.7 m, 2.4 m, 1.6 m, 0.46 m
282 and 0.34 m (Fig. 6E). An additional period is recorded with a confidence level exceeding 95%
283 at 0.56 m. The COCO method applied to Interval 2 of CPG-1 shows a highly significant
284 correlation at a sedimentation rate of 1.9 cm/kyr. Additional significant correlations are

285 observed around 2.2 cm/kyr, 2.5 cm/kyr and 1.3 cm/kyr with however less confidence (Fig.
286 6F).

287 **4.3.2 CPG-2**

288 The 2π -MTM spectrum performed along CPG-2 shows the presence of significant periods with
289 a confidence level higher than 99% at 20 m, 10 m, 6.9 m, 3.6 m, 1.5 m, 1.0 m and 0.74 m. In
290 addition, periods at 2.2 m and 1.2 m exceed the 95 % confidence level (Fig. 8A). A spectrogram
291 was performed on 40-m width windows to focus on the lowest frequencies (Fig. 9C). Another
292 spectrogram was performed on 15-m width windows after filtering the lowest frequencies with
293 a Taner low-pass filter in order to focus on the high frequencies (frequency cut:
294 0.1319243cycles/m, Fig. 9D). The spectrogram focused on the low frequencies shows a low-
295 amplitude band with periods of 15 and 8 m from the base of the series to level 25 m (Fig. 9C).
296 These low frequencies show then a bifurcation to high-amplitude period of 30 m and a lower-
297 amplitude period of 10 m. This bifurcation is observed from level 25 m to 70 m (Fig. 9C). This
298 band then stabilizes to periods ranging from 26 m to 20 m from level 70 m to the top of the
299 series (Fig. 9C). An additional band is recorded with periods increasing from 3.2 m to 4.2 m,
300 from the base of the series to level 35 m. Periods of 6.8 to 3.6 m are observed from level 35 m
301 to 80 m (Fig. 9C) and periods of 5.1 to 3.3 m are observed from level 85 m to the top of CPG-
302 2 (Fig. 9C). At higher frequencies, periods around 1.5 m 0.74 m are recorded throughout CPG-
303 2 with low amplitudes (Fig. 9D).

304 The COCO analysis along the CPG-2 shows highest correlations at (p -value $<1\times 10^{-3}$) at
305 sedimentation rates of 2.5 cm/kyr, 3.3 cm/kyr, 5.3 cm/kyr and 7 cm/kyr (Fig.8B). The eCOCO
306 analysis performed on 40-m width windows shows significant correlations between the spectra
307 of the sedimentary and astronomical series at the sedimentation rate around 2.4 cm/kyr, 3.3
308 cm/kyr from levels 0 m to 30 m (Fig. 9E). From level 30 m to the top of the section, most

309 significant correlation is observed at sedimentation rates decreasing from 7.2 cm/kyr at level
310 27 m to 4 cm/kyr at the top of CPG-2.

311 Based on the evolutive spectral and eCOCO analyses, CPG-2 was divided into an interval from
312 0 to 30 m, in which the most likely sedimentation rate appears to be around 3 cm/kyr, and from
313 20 m to the top of CPG-2, in which the most likely sedimentation rate is higher and
314 progressively decreases throughout the interval (Fig. 9E). The 2π -MTM spectrum performed
315 on Interval 1 of CPG-2 (from 0 m to 30 m), show significant periods with confidence levels
316 higher than 99% observed at 7.5 m, 2.1 m, 1.0 m and 0.73 m (Fig. 8C). Two periods exceeding
317 the 95 % confidence level are observed at 1.6 m and 0.33 m, and two periods exceeding the 90
318 % confidence level are observed at 0.47 m and 0.37 m. The COCO analysis performed on
319 Interval 1 of CPG-2, indicates that the highest significant correlations (p -value $<1\times 10^{-3}$) is at a
320 sedimentation rate of 2.5 cm/kyr (Fig. 8D). In Interval 2 of CPG- 2 (from 20 m to the top), the
321 2π -MTM spectrum shows spectral peaks at 22 m, 7.3 m, 3.7 m, 1.5 m, 0.94 m, 0.83 m and 0.75
322 m exceeding the 99 % confidence level (Fig. 8E). The COCO analysis shows a high significant
323 correlation (p -value $<1\times 10^{-3}$) at sedimentation rates at 5.5 cm/kyr, and 7.1 cm/kyr (Fig. 8F).

324 5. Discussion

325 5.1. Interpretation of the sedimentary cycles for CPG-1

326 The signal processing along the CPG-1 indicates two intervals with an average sedimentation
327 rate of 3 cm/kyr from 0 to 30 m and of 2 cm/kyr from 30 m to the top of the series (Fig. 7E). In
328 previous spectral analyses, an average sedimentation rate of 3 cm/kyr was estimated for the
329 upper Aptian in hemipelagic deposits of the Vocontian Basin, SE France (Heimhofer et al.,
330 2004; Köbller et al., 2001). The present analysis confirms and refines these previous estimates.
331 From COCO, eCOCO and spectral analyses, the thickness of the 405-kyr eccentricity cycle
332 evolves from an average of 14 m in Interval 1 of CPG-1 to 8.7 m in Interval 2 of CPG-1. The

333 thickness of the 100-kyr eccentricity cycle evolves from 3.4 m in Interval 1 to ~2 m in Interval
334 2 (with a range from 2.7 to 1.6 m). The thickness of the precession cycles evolves from 0.65 m
335 in Interval 1 to 0.46 m in Interval 2 (Fig. 7). The 405-kyr eccentricity cycle was extracted using
336 a Taner lowpass filter performed on the whole of CPG-1 with a higher frequency cut of 0.1648
337 cycles/m (Fig. 7B). In addition, the 100-kyr eccentricity band was extracted using Taner
338 bandpass filters with lower and higher frequency cuts of 0.1833 and 0.6000 cycles/m in Interval
339 1, and lower and higher frequency cuts of 0.2365 and 0.7095 cycles/m in Interval 2. The filter
340 of the 405-kyr eccentricity cycles shows 4 repetitions at CPG-1, implying a total duration of
341 the sampled interval of 2.38 myr and duration of the interval from the base of the Jacob to the
342 base of the Kilian event of 1.55 myr.

343 A recent dataset published by Charbonnier et al. (2023) estimates from an eCOCO analysis a
344 sedimentation rate of 4.5 cm/kyr in CPG-1, which leads to a duration of 0.8 myr between the
345 Jacob and Kilian events. Charbonnier et al. (2023) used a window size of 60 m to perform the
346 eCOCO analysis. The most likely sedimentation rate calculated from this approach is 5.8
347 cm/kyr, decreasing to 4.3 cm/kyr in the topmost 60 m of the series (Fig. 10D). However, a TF-
348 WFFT applied on the series with 15-m width windows shows that the periods of the highest
349 frequencies evolve from 1.3 to 1.6 m from the bottom of L5 to 300 m, and then decrease down
350 to 0.3-0.4 m in the topmost 20 m of the series (Fig. 10C, see also Fig. S1D in the electronic
351 supplement). Another eCOCO analysis applied on 25-m width windows (Fig. 10E) shows most
352 likely sedimentation of 4.0 to 6.0 cm/kyr from 300 to 320 m, 3.4 cm/kyr 330 to 375 m and 2.2
353 cm/kyr in the topmost part of the series. We performed three 2π -MTM analyses from the base
354 of the series to 320 m (Interval 1), from 315 m to 365 m (Interval 2) and from 360 m to the top
355 of the series (Interval 3; Figs. 10F-H).

356 The 2π -MTM spectrum of Interval 1 shows periods at 22 m, attributed to the 405-kyr
357 eccentricity cycle, from 6.7 m to 4.0 m, attributed to the 100-kyr eccentricity cycle, from 2.5 to

358 1.9 m, attributed to the obliquity, and from 1.6 m to 0.85 m, attributed to the precession (Fig.
359 10F). The 2π -MTM spectrum of Interval 2 shows periods at 17 m, attributed to the 405-kyr
360 eccentricity cycle, from 3.8 m to 2.2 m, attributed to the 100-kyr eccentricity cycle, from 1.7 to
361 1.0 m, attributed to the obliquity, and from 0.7 m to 0.50 m, attributed to the precession (Fig.
362 10G). The 2π -MTM spectrum of Interval 3 shows periods at 8.6 m, attributed to the 405-kyr
363 eccentricity cycle, from 2.2 m to 1.5 m, attributed to the 100-kyr eccentricity cycle, and from
364 0.55 m to 0.29 m, attributed to the precession (Fig. 10H). These spectra performed on these
365 intervals agree with the broad variations in the sedimentation rates calculated from eCOCO
366 with window sizes of 25 m.

367 This comparison highlights that eCOCO analyses, as well as evolutive FFTs, are sensitive to
368 the sizes of the windows chosen. Long window sizes are efficient to calculate large
369 sedimentation rates. However, they cannot capture their rapid variations within the sedimentary
370 series. Conversely, short window sizes can be efficient to capture these rapid variations in the
371 sedimentation rates. Thus, by focusing on Col de Pré-Guittard series, our study is able to
372 observe this decrease in the sedimentation in the last 20 m of CPG-1.

373 **5.2. Interpretation of the sedimentary cycles for CPG-2**

374 The signal processing along the CPG-2 indicates an average sedimentation rate of 3 cm/kyr
375 from 0 to 30 m and a sedimentation rate varying from 4 cm/kyr to 7 cm/kyr in the remaining
376 part of the series (Fig. 9E). From COCO, eCOCO and spectral analyses, the thickness of the
377 405-kyr eccentricity cycle evolves from an average of 13 m from level 0 to level 43 m, an
378 average of 11 m from level 43 m to level 54 m, and an average thickness of 23 m in the
379 remaining part of the studied series (Fig. 9B). The 100-kyr eccentricity cycle has a thickness
380 ranging from 3 to 4 m from the base of the series to level 32 m, and thicknesses ranging from
381 7 m to 3 m from level 32 m to level. The obliquity is well expressed from the base of the series
382 to level 32 m. Then the precession has higher amplitude with thicknesses ranging from 1.5 m

383 to 0.7 m to the top of the series. Our calibration shows that 405-kyr eccentricity cycles Ab405-
384 3 and Ab405-4 contain six repetitions of the 100-kyr eccentricity altogether. This interval
385 contains the glauconitic sandstone layer associated to a short-term hiatus which duration could
386 be assessed at 200 kyr provided that no complete 405-kyr eccentricity has been erased.

387 The 405-kyr eccentricity cycle was extracted using a Taner lowpass filter with a higher
388 frequency cut of 0.1648 cycles/m. The 100-kyr eccentricity cycle was extracted using a Taner
389 bandpass filter with a lower and higher frequency cut of 0.2167 cycles/m and 0.5667 cycles/m
390 in Interval 1 and lower and higher frequency cuts of 0.1251 cycles/m and 0.3527 cycles/m in
391 Interval 2. The filter of the 405-kyr eccentricity cycles shows 6 repetitions at CPG-2 and implies
392 a minimum duration of deposit of 2.63 myr. This duration is qualified as “minimum” to account
393 for the potential hiatus linked to the glauconitic sandstone layer. The minimum duration
394 between the base of the Kilian and the base of the Paquier levels is assessed at 1.62 myr and
395 the duration between the Paquier and the Leenhardt levels is assessed at 0.93 myr.

396 Recent CaCO_3 data have been published from the Les Briers section, in the eastern part of the
397 Vocontian Basin from the Kilian to Paquier levels (Bodin et al., 2023). The data have been
398 measured with a median sample distance of 1 m. Assuming an average sedimentation rate of
399 3.8 cm/kyr between the Kilian and Paquier events at Les Briers (60 m between these events,
400 duration: 1.6 myr), this represents a time of 26 kyr, enough to detect the 405-kyr eccentricity
401 cycle at least. The CaCO_3 signal is selected for performing spectral analyses in Les Briers as it
402 is inversely correlated to the MS signal in the Marnes Bleues Formation (see Fig. 4 and Ghirardi
403 et al., 2014).

404 The CaCO_3 signal was linearly interpolated every 50 cm and detrended applying a LOWESS
405 with a coefficient of 0.3 (Fig. 11C). The 2π -MTM spectrum of the detrended CaCO_3 signal
406 shows spectral peaks at 17 m, exceeding the 99 % CL (Fig. 12), which represents a duration of
407 0.4 myr, assuming a sedimentation rate of 3.8 cm/kyr. The 17-m peak could thus represent the

408 405-kyr eccentricity cycle. The Taner lowpass filter of the peak at 17 m shows 4 repetitions
409 between the Kilian and the Paquier, in agreement with the finding at CPG-2(Fig. 11D). This
410 suggests that the hiatus associated with the calciturbidite event did not erase a complete 405-
411 kyr eccentricity cycle and thus did not affect the duration estimates between the Kilian and
412 Paquier events.

413 **5.3 Forcing factors of Aptian–Albian black shales**

414 Our astrochronology based on 405-kyr filter recorded at CPG-1 and CPG-2 shows that eleven
415 repetitions of the 405-kyr eccentricity cycles are recorded in the studied interval. The Jacob
416 Level is located at the boundary between E405-1 and E405-2 (Fig. 7), while the Leenhardt
417 Level is located less than 0.1 myr below the top of cycle Ab405-6 (Fig. 9), leading to a duration
418 from the base of the Jacob Event to the top of the Leenhardt Event, so-called OAE1b interval,
419 of 4.03 myr. Interestingly, the duration of the OAE1b interval calculated here is in close
420 agreement to the duration of 4.27 myr proposed for the OAE 1b interval in the Geologic Time
421 Scale 2020 (Gale et al., 2020), suggesting again that the hiatus related to the glauconitic
422 sandstone did not erase a complete 405-kyr eccentricity cycle. The duration between the four
423 events (Jacob, Kilian, Paquier and Leenhardt) are respectively 1.55 myr, 1.62 myr and 0.93
424 myr. These durations do not follow the long eccentricity and obliquity cycles (2.4 myr, and 1.2
425 myr, respectively). This suggests that the long orbital cycles are not responsible for the
426 inception of the main anoxic events of the OAE 1b interval. However, these four events all
427 locate just below a maximum in the filter of the 405-kyr eccentricity cycle, suggesting that this
428 eccentricity could have impacted, in addition to another forcing factor, the onset of the events.

429 Caillaud et al. (2022) attribute the concomitant accumulation of organic matter during the
430 oceanic anoxic events (OAE 1b) to various parameters such as productivity, sea level,
431 sedimentation, and accumulation rates with the influence of regional factors. In Poggio le

432 Guaine (Umbria-Marche Basin, central Italy), two negative spikes in Os isotopes below the
433 Kilian level, together with mercury enrichments in the OAE 1b interval, suggest a link between
434 this event and the multi-phase emplacement of the southern Kerguelen plateau in the late
435 Aptian-early Albian (Matsumoto et al., 2020; Sabatino et al., 2018). The emplacement of the
436 southern Kerguelen plateau (Indian Ocean) coincides with the Aptian-Albian transition (113
437 Ma) and correspond to the production of 2.5×10^7 km³ of mafic crust (Coffin et al., 2002).
438 Conversely, Benamara et al. (2020) show a lack of significant Hg enrichment in the Paquier
439 Level suggesting that this event is not linked to Kerguelen plateau LIP activity. Finally,
440 Bracquart et al. (2022) noted that in DSDP Site 545 off Morocco, mercury enrichment occurred
441 *ca.* 5-6 m below the Kilian Event, corresponding to *ca.* 200-250 kyr, assuming a thickness of
442 40 m between the Kilian and Jacob events and our time scale (Herrle et al., 2004). These two
443 last studies show that the volcanism is not the sole forcing factor to the onset of these anoxic
444 episodes. Hence, Wang et al. (2022) showed that pronounced global deoxygenation period
445 occurred only during the Paquier event, which was related to warmer climate and increased
446 nutrient levels linked to the long-term influence of the Kilian event triggering volcanism
447 modulated by orbital parameters. In a context of a series of volcanic pulses linked for instance
448 to the emplacement of the Kerguelen Plateau, the modification of the seasonality may act as an
449 additional forcing factor which contributed the climate system to pass a threshold leading to
450 widespread anoxia. Jovane et al. (2006) and Leandro et al. (2022) presumed that the continental
451 runoff occurred during wetter climate phases which occurred during the seasonal variability
452 during eccentricity maxima.

453 **5.4. Implications for the timescale of the Aptian Stage**

454 The age of the top of the Aptian Stage is constrained by the U-Pb age of 113.1 ± 0.3 Ma obtained
455 on zircon crystals from the Vöhrum bentonite, approximately 100 kyr above the Aptian-Albian
456 boundary (Selby et al., 2009; Gale et al., 2020). The astrochronology from the Valanginian to

457 the earliest Aptian in the Tethys area anchored to CA-ID-TIMS U-Pb ages in the Neuquén
458 Basin led to an age of the base of the Aptian Stage of 121.15 ± 0.31 Ma (Martinez et al., 2023).
459 Radiometric ages suggest an age of magnetochron M0r of 121.2 ± 0.5 Ma (He et al., 2008;
460 Zhang et al., 2021). Bio- and chemostratigraphic correlations suggest that magnetochron M0r
461 is equivalent in time to the *Imerites giraudi* and *Martellites sarasini* Tethyan ammonite zones
462 (Aguado et al., 2022), which age range from 122.01 to 121.15 Ma (Martinez et al., 2023). The
463 radiometric ages measured at the end of the Barremian Stage thus agree (He et al., 2008; Zhang
464 et al., 2021) with the astrochronology independently performed in the Tethys area (Martinez et
465 al., 2023). These ages constrain a duration of the Aptian Stage of 8.0 myr.

466 The astrochronology of the Piobbico core in central Italy (Huang et al., 2010) suggests the
467 existence of four or five 405-kyr eccentricity cycles from the base of the Jacob level to the top
468 of the Kilian levels implying a duration of 1.6 to 2.0 myr between these two events (Fig. 13A).
469 A shorter duration of 0.8 myr is proposed by Leandro et al. (2022) and Charbonnier et al. (2023)
470 based on the astronomical calibration of Poggio le Guaine (PLG) in Italy (Fig. 13C) and Col de
471 Pré-Guittard. Our astronomical calibration agrees best with the option of Huang et al. (2010) at
472 1.6 myr (Fig. 13B), suggesting a possible condensation/hiatus, or decreased sedimentation rate
473 not detected by Leandro et al. (2022) in this specific interval at PLG, and a decreased
474 sedimentation rate in the upper part of CPG-1 not detected in Charbonnier et al. (2023), as
475 discussed in section 5.1 (see also Figs. S1-S3 in the electronic supplement). However, the
476 duration of the whole Aptian of 13.4 myr proposed by Huang et al. (2010) does not agree with
477 the duration of 8 myr discussed above. The astrochronology of Charbonnier et al. (2023)
478 suggests a duration of 9.6 myr of the Aptian Stage assuming a duration of 0.8 myr between the
479 Jacob and Kilian events. Adding two 405-kyr eccentricity cycles would lead to a duration of
480 10.4 myr, which appears as well too long compared to the duration obtained from radiometric
481 ages.

482 Conversely, Leandro et al. (2022) identified 18 repetitions of the 405-kyr eccentricity cycles
483 and estimated the duration from the Kilian Event to magnetochron M0r as 7.2 myr. Adding two
484 repetitions of the 405-kyr cycle between the Kilian and the Jacob event to the age model of
485 Leandro et al. (2022) leads to a duration of 8 myr from the Kilian Event to chron M0r.
486 Anchoring this duration to the age of 113.2 Ma proposed in the Geologic Time Scale 2020 leads
487 to an age of magnetochron M0r of 121.2 Ma, which is in falls within the radiochronology
488 proposed by He et al. (2008). Our data thus contribute to the establishment of an increasingly
489 precise timescale in the Aptian Stage.

490

491 **Conclusions**

492 An astronomical calibration is performed from a high-resolution magnetic susceptibility signal
493 in the Col de Pré-Guittard section, GSSP of the Albian Stage in the Vocontian Basin, France.
494 The section records the influence of the eccentricity and precession cycles mainly. The 405-kyr
495 cycle is well-identified and leads to estimate a duration of the interval covering the Jacob to
496 Leenhardt events to 4.03 myr. The duration of the Jacob-Kilian interval, Kilian-Paquier interval
497 and Paquier-Leenhardt interval are respectively 1.55, 1.62 and 0.93 myr. The occurrence of
498 these organic matter rich events (Jacob, Kilian, Paquier and Leenhardt) is partly controlled by
499 the eccentricity cycle, all four events being located around the maximum of filter 405-kyr
500 eccentricity. However, the orbital forcing on the occurrence of these events is not the sole factor
501 explaining the onset of these events and it is likely that both volcanism and orbitally-controlled
502 change in seasonality made the climate system to pass a threshold leading to widespread anoxia.
503 Anchoring our timescale to the astrochronology of the Aptian of Leandro et al. (2022) and the
504 U-Pb age of Selby et al. (2009) near the Aptian-Albian boundary, we estimate the duration from
505 the Kilian Event to magnetochron M0r to 8 myr, and suggest an age of 121.2 Ma for

506 magnetochron M0r, which is in line with the radiometric data produced in the late Barremian
507 and magnetochron M0r.

508

Journal Pre-proof

509

510 **Acknowledgments**

511 The project was funded by MOPGA program (Make Our Planet Great Again), project SAD
 512 METOX from Région Bretagne, CNRS MITI Le Temps AstroCarb, and Défis Scientifiques
 513 program from Université de Rennes 1. We warmly thank Danny Boué, Anne Lise Santoni,
 514 Pierrick Roperch and Léa Beaubant for their help respectively on the field and in the laboratory.
 515 The authors are very grateful to the Editor Dr. Eduardo Koutsoukos and for the anonymous
 516 reviewers for their constructive comments, which led to improvements of the final version of
 517 the manuscript.

518 **References**

- 519 Aguado, R., Company, M., O'Dogherty, L., Sandoval, J., Martinez, M., 2022. New insights into the Barremian–
 520 lower Aptian calcareous nannofossils of the Mediterranean Tethys: Chronostratigraphic and
 521 paleobiogeographic implications. *Marine Micropaleontology* 173, 102114.
 522 <https://doi.org/10.1016/j.marmicro.2022.102114>.
- 523 Arnaud, H., Arnaud-Vanneau, A., Godet, A., Adatte, T., Massonnat, G., 2017. Barremian platform carbonates
 524 from the eastern Vercors Massif, France: Organization of depositional geometries. *AAPG Bulletin* 101,
 525 485–493. <https://doi.org/10.1306/011817DIG17027>.
- 526 Barrier, E., Vrielynck, B., Brouillet, J.-F., Brunet, M.-F., 2018. Paleotectonic
 527 Reconstruction of the of the Central Tethyan Realm. CCGM-CGMW, Paris.
- 528 Benamara, A., Charbonnier, G., Adatte, T., Spangenberg, JE., Föllmia, KB., 2020. Precession-driven monsoonal
 529 activity controlled the development of the early Albian Paquier oceanic anoxic event (OAE1b): Evidence
 530 from the Vocontian Basin, SE France. *Palaeogeography, Palaeoclimatology, Palaeoecology* 537, 109406.
 531 <https://doi.org/10.1016/j.gloplacha.2022.103959>.
- 532 Bodin, S., Meissner, P., Janssen, N. M., Steuber, T., Mutterlose, J., 2015. Large igneous provinces and organic
 533 carbon burial: Controls on global temperature and continental weathering during the Early Cretaceous.
 534 *Global and Planetary Change* 133, 238–253. <https://doi.org/10.1016/j.gloplacha.2015.09.001>.
- 535 Bodin, S., Charpentier, M., Ullmann, C.V., Rudra, A., Sanei, H. Carbon cycle during the late Aptian-deposits
 536 Albian OAE 1b : A focus on the Kilian-Paquier levels interval. *Global and Planetary Change* 222, 104074.
 537 <https://doi.org/10.1016/j.gloplacha.2023.104074>.
- 538 Bottini, C., and Erba, E., 2018. Mid-Cretaceous paleoenvironmental changes in the western Tethys. *Climate of the*
 539 *Past Discussions*, 1–23. <https://doi.org/10.5194/cp-14-1147-2018>.
- 540 Bottini, C., Erba, E., Tiraboschi, D., Jenkyns, HC., Schouten, S., Sinninghe Damsté, JS., 2015. Climate variability
 541 and ocean fertility during the Aptian Stage. *Climate of the Past* 11, 383–402. <https://doi.org/10.5194/cp-11-383-2015>.
- 542 Bracquart, E., Charbonnier, G., Garel, S., Munier, T., Adatte, T., Danzelle, J., 2022. New evidences of subaerial
 543 volcanism as a trigger for the Kilian event (Aptian-Albian transition) and major climatic changes from
 544 offshore Morocco (DSDP Site 545). *Global and Planetary Change* 218, 103959.
 545 <https://doi.org/10.1016/j.gloplacha.2022.103959>.

- 547 Bréhéret, J.G., 1985. Indices d'un événement anoxique étendu à la Téthys alpine, à l'Albien inférieur (événement
548 Paquier). *C.R. Acad. Sci., Paris* 300, II, 8, 355–358.
- 549 Bréhéret, J.G., 1988. Episodes de sédimentation riche en matière organique dans les marnes bleues d'âge Aptien
550 et Albien de la partie pélagique du bassin Vocontien. *Bull. Soc. Géol. Fr.* 8, 349–356.
551 <https://doi.org/10.2113/gssgfbull.IV.2.349>.
- 552 Bréhéret, J.G., 1997. L'Aptien et l'Albien de la Fosse vocontienne (des bordures au bassin). *Évolution de la*
553 *sédimentation et enseignements sur les événements anoxiques. Société géologique du Nord* 25, 644.
- 554 Bréhéret, J.G and Brumsack, H-J., 2000. Barite concretions as evidence of pauses in sedimentation in the Marnes
555 Bleues Formation of the Vocontian Basin (SE France). *Sedimentary Geology* 130, 205–228.
556 [https://doi.org/10.1016/S0037-0738\(99\)00112-8](https://doi.org/10.1016/S0037-0738(99)00112-8).
- 557 Caillaud, A., Quijada, M., Hlohowskyj, SR., Chappaz, A., Bout-Roumazeilles, V., Reynaud, J-Y., Riboulleau, A.,
558 Baudin, F., Adatte, T., Ferry, J-N., Tribouvillard, N., 2022. Assessing controls on organic matter
559 enrichments in hemipelagic marls of the Aptian-Lower Albian Blue Marls of the Vocontian Basin
560 (France): an unexpected variability observed from multiple “organic-rich” levels. *BSGF – Earth Sciences*
561 *Bulletin* 193, 2. <https://doi.org/10.1051/bsgf/2022001>.
- 562 Charbonnier, G., Boulila, S., Spangenberg, J.E., Vermeulen, J., Galbrun, B., 2023. Astrochronology of the Aptian
563 stage and evidence for the chaotic motion of Mercury. *Earth and Planetary Science Letters* 610, 118104.
564 <https://doi.org/10.1016/j.epsl.2023.118104>.
- 565 Cleveland, W.S., 1979. Robust Locally Regression and Smoothing Scatterplots. *Journal of American Statistical*
566 *Association* 74, 829–836.
- 567 Coccioni, R., Sabatino, N., Frontalini, F., Gardin, S., Sideri, M., Sprovieri, M., 2014. The
568 neglected history of Oceanic Anoxic Event 1b: insights and new data from the Poggio le Guaine section
569 (Umbria–Marche Basin). *Stratigraphy* 11, 245–282.
- 570 Coffin, M.F., Pringle, M.S., Duncan, R.A., Gladchenko, T.P., Storey, M., Müller, R.D., and Gahagan, L.A., 2002,
571 Kerguelen hotspot magma output since 130 Ma. *Journal of Petrology* 43, 1121–1137.
572 <https://doi.org/10.1093/petrology/43.7.1121>.
- 573 Coentyn, P., Deconinck, J.F., Pellenard, P., Amédro, F., Bruneau, L., Chenot, E., Matrimon, B.,
574 Huret, E., Landrein, P., 2020. Environmental and climatic controls of the clay mineralogy of Albian
575 deposits in the Paris and Vocontian Basins (France). *Cretaceous Research* 108, 104342.
576 <https://doi.org/10.1016/j.cretres.2019.104342>.
- 577 Dercourt, J., Ricou, L.E., Vrielynck, B., 1993. *Atlas Tethys Paleoenvironmental Maps*. Gauthier-Villars, Paris.
- 578 Erba, E., 1994. Nannofossils and superplumes. The early Aptian ‘nannoconid crisis’. *Paleoceanography* 9, 483–
579 501. <https://doi.org/10.1029/94PA00258>.
- 580 Erbacher, J., Hemleben, C., Huber, B.T., Markey, M., 1999. Correlating environmental changes during early
581 Albian oceanic anoxic event 1B using benthic foraminiferal paleoecology. *Marine Micropaleontology* 38,
582 7–28. [https://doi.org/10.1016/S0377-8398\(99\)00036-5](https://doi.org/10.1016/S0377-8398(99)00036-5).
- 583 Erbacher, J. and Thurow, J., 1997. Influence of oceanic anoxic events on the evolution of mid-Cretaceous
584 radiolaria in the North Atlantic and western Tethys. *Mar. Micropaleontol* 30, 139–158.
585 [https://doi.org/10.1016/S0377-8398\(96\)00023-0](https://doi.org/10.1016/S0377-8398(96)00023-0).
- 586 Föllmi, K.B., 2012. Early Cretaceous life, climate and anoxia. *Cretaceous Research* 35, 230–
587 257. <https://doi.org/10.1016/j.cretres.2011.12.005>.
- 588 Friedrich, O., 2010. Benthic foraminifera and their role to decipher paleoenvironment during mid-Cretaceous
589 Oceanic Anoxic Events -the “anoxic benthic foraminifera” paradox. *Revue de micropaléontologie* 53,
590 175–192. <https://doi.org/10.1016/j.revmic.2009.06.001>.
- 591 Friès, G. and Parize, O., 2003. Anatomy of ancient passive margin slope systems: Aptian gravity-driven deposition
592 on the Vocontian palaeomargin, western Alps, south-east France. *Sedimentology* 50, 1231–1270.
593 <https://doi.org/10.1111/j.1365-3091.2003.00601.x>.
- 594 Gale, A. S., Mutterlose, J., Batenburg, S. In *Geologic Time Scale 2020* (eds Gradstein, F. M. et al.) 1023–1068.
595 <https://doi.org/10.1016/B978-0-12-824360-2.00027-9>.
- 596 Ghirardi, J., Deconinck, J.F., Pellenard, P., Martinez, M., Bruneau, L., Amiotte- Suchet, P., Pucéat, E., 2014.
597 Multi-proxy orbital chronology in the aftermath of the Aptian Oceanic Anoxic Event 1a:
598 Palaeoceanographic implications (Serre Chaitieu section, Vocontian Basin, SE France). *Newsletters on*
599 *Stratigraphy* 47, 247–262. <https://10.1127/0078-0421/2014/0046>.
- 600 He, H., Pan, Y., Tauxe, L., Qin, H., Zhu, R., 2008. Toward age determination of the M0r (Barremian–Aptian
601 boundary) of the early Cretaceous. *Phys. Earth Planet. Inter.* 169, 41–48.
602 <https://doi.org/10.1016/j.pepi.2008.07.014>.

- 603 Heimhofer, U., Hochuli, P.A., Herrle, J.O., Andersen, N., Weissert, H., 2004. Absence of major vegetation and
604 palaeoatmospheric pCO₂ changes associated with oceanic
605 anoxic event 1a (early Aptian, SE France). *Earth and Planetary Science Letters* 223, 303–318.
606 <https://doi.org/10.1016/j.epsl.2004.04.037>.
- 607 Herrle, J.O., and Mutterlose, J., 2003. Calcareous nannofossils from Aptian–Lower Albian of southeast France:
608 palaeoecological and biostratigraphic implications: *Cretaceous Research* 24, 1–22.
609 [https://doi.org/10.1016/S0195-6671\(03\)00023-5](https://doi.org/10.1016/S0195-6671(03)00023-5).
- 610 Herrle, J.O., Köbller, P., Friedrich, O., Erlenkeuser, H., Hemleben, C., 2004. High-resolution carbon isotope
611 records of the Aptian to Lower Albian from SE France and the Mazagan Plateau (DSDP site 545): a
612 stratigraphic tool for paleoceanographic and paleobiologic reconstruction, *Earth and Planetary Science*
613 *Letters* 218, 149–161. [https://doi.org/10.1016/S0012-821X\(03\)00646-0](https://doi.org/10.1016/S0012-821X(03)00646-0).
- 614 Herrle, J.O., Schröder-Adams, C.J., Davis, W., Pugh, A.T., Galloway, J.M., Fath, J., 2015. Mid- Cretaceous igh
615 Arctic stratigraphy, climate, and Oceanic anoxic events. *Geology* 43, 403–406.
616 <https://doi.org/10.1130/G36439.1>.
- 617
- 618 Huang, C., Hinnov, L., Fischer, A.G., Grippo, A., Herbert, T., 2010. Astronomical tuning of the Aptian Stage from
619 Italian reference sections. *Geology* 30, 899–902. <https://doi.org/10.1130/G31177.1>.
- 620 Huber, B.T., Leckie, R.M., 2011. Planktic foraminiferal turnover across deep-sea Aptian/Albian boundary
621 sections. *Journal of Foraminiferal Research* 41, 53–95. <https://doi.org/10.2113/gsjfr.41.1.53>.
- 622 Jovane, L., Florindo, F., Sprovieri, M., P' alike, H., 2006. Astronomic calibration of the late Eocene/early
623 Oligocene Massignano section (Central Italy). *Geochem. Geophys. Geosyst.* 7, 1–10.
624 <https://doi.org/10.1029/2005GC001195>.
- 625 Kennedy, W.J., Gale, A.S., Bown, P.R., Caron, M., Davey, R.J., Gröcke, D., and Wray, D.J., 2000. Integrated
626 stratigraphy across the Aptian–Albian boundary in the Marnes Bleues, at the Col de Pré-Guittard,
627 Arnayon (Drôme), and at Tartonne (Alpes-de-Haute-Provence), France, a candidate Global boundary
628 Stratotype Section and Point for the base of the Albian Stage. *Cretaceous Research* 21, 591–720.
629 <https://doi.org/10.1006/cres.2000.0223>.
- 630 Kennedy, J.W., Gale, A.S., Huber, B.T., Petrizzo, M.R., Bown, P., Jenkyns, H.C., 2017. The Global Boundary
631 Stratotype Section and Point (GSSP) for the base of the Albian Stage, of the Cretaceous, the Col de Pré-
632 Guittard section, Arnayon, Drôme, France. *Episodes* 40, 177–188.
633 <https://doi.org/10.18814/epiugs/2017/v40i3/017021>.
- 634 Köbller, P., Herrle, JO., Appel, E., Erbacher, J., Hemleben, C., 2001. Magnetic records of climatic cycles from
635 mid-cretaceous hemipelagic sediments of the Vocontian Basin, SE France. *Cretaceous Research* 22,
636 321–331. <https://doi.org/10.1006/cres.2001.0256>.
- 637 Laskar, J., Robutel, P., Joutel, F., Gastineau, M., Correia, A.C.M., Levrard, B., 2004. A long-term numerical
638 solution for the insolation quantities of the Earth. *Astron. Astrophys.* 428, 261–285.
639 <https://doi.org/10.1051/0004-6361:20041335>.
- 640 Leandro, C.G., Savian, J.F., Kochhann, M.V.L., Franco, D.R., Coccioni, R., Frontalini, F., Gardin, S., Jovane, L.,
641 Figueiredo, M., Tedeschi, L.R., Janikan, L., Almeida, R. P., Trindade, R. P. F., 2022. Astronomical
642 tuning of the Aptian stage and its implications for age recalibrations and paleoclimatic events. *Nat*
643 *Commun* 13, 2941. <https://doi.org/10.1038/s41467-022-30075-3>.
- 644
- 645 Li, M., Hinnov, L., Kump, L., 2019. Acycle: Time-series analysis software for paleoclimate research and education.
646 *Computers & Geosciences* 127, 12–22.
- 647 Mann, M.E., Lees, J.M., 1996. Robust estimation of background noise and signal detection in climatic time series.
648 *Clim. Change* 33, 409–445. <https://doi.org/10.1007/BF00142586>.
- 649 Martinez, M., Aguirre-Urreta, B., Dera, G., Lescano, M., Omarini, J., Tunik, M., O'Dogherty, L., Aguado, R.,
650 Company, M., Bodin, S., 2023. Synchrony of carbon cycle fluctuations, volcanism and orbital forcing
651 during the Early Cretaceous. *Earth-Science Reviews* 239, 104356.
652 <https://doi.org/10.1016/j.earscirev.2023.104356>.

- 653 Martinez, M., Deconinck, J.F., Pellenard, P., Riquier, L., Company, M., Reboulet, S., Moiroud, M., 2015.
 654 Astrochronology of the Valanginian–Hauterivian stages (Early Cretaceous): chronological
 655 relationships between the Paraná–Etendeka large igneous province, the Weissert and the Faraoni events.
 656 *Glob. Planet. Change* 131, 158–173. <https://doi.org/10.1016/j.gloplacha.2015.06.001>.
- 657 Matsumoto, H., Kuroda, J., Coccioni, R., Frontalini, F., Sakai, S., Ogawa, N.O., Ohkouchi, N., 2020. Marine Os
 658 isotopic evidence for multiple volcanic episodes during Cretaceous Oceanic Anoxic Event 1b. *Sci. Rep.*
 659 10, 12601. <https://doi.org/10.1038/s41598-020-69505-x>.
- 660 McAnena, A., Flögel, S., Hofmann, P., Herrle, J.O., Griesand, A., Pross, J., Talbot, H.M., Rethemeyer, J.,
 661 Wallmann, K., Wagner, T., 2013. Atlantic cooling associated with a marine biotic crisis during the mid-
 662 Cretaceous period *Nat. Geosci.* 6, 558–561. <https://doi.org/10.1038/ngeo1850>.
- 663 Millán, M.I., Weissert, H.J., López-Horgue, M.A., 2014. Expression of the late Aptian cold snaps and the OAE1b
 664 in a highly subsiding carbonate platform (Aralar, Northern Spain). *Palaeogeogr. Palaeoclimatol.*
 665 *Palaeoecol.*, 411, 167–179. <https://doi.org/10.1016/j.palaeo.2014.06.024>.
- 666 Mutterlose, J., Bornemann, A., Herrle, J., 2009. The Aptian–Albian cold snap: evidence for “mid” Cretaceous
 667 icehouse interludes. *N. Jb. Geol. Paläont.* 252, 217–225. [10.1127/0077-7749/2009/0252-0217](https://doi.org/10.1127/0077-7749/2009/0252-0217).
- 668 Price, G.D., 1999. The evidence and implications of polar ice during the Mesozoic. *Earth Sci. Rev.* 48, 183–210.
 669 [https://doi.org/10.1016/S0012-8252\(99\)00048-3](https://doi.org/10.1016/S0012-8252(99)00048-3).
- 670 Rodríguez-López, J-p., C-L., Pardo, G., Meléndez, N., Soria A-R., Skillinga, I., 2016. Glacial dropstones in the
 671 western Tethys during the late Aptian–early Albian cold snap: Palaeoclimate and palaeogeographic
 672 implications for the mid-Cretaceous. *Palaeogeography, Palaeoclimatology, Palaeoecology*, 452, 11–27.
 673 <https://doi.org/10.1016/j.palaeo.2016.04.004>.
- 674 Prokopenko, A.A., Hinnov, L.A., Williams, D.F., Kuzmin, M.I., 2006. Orbital forcing of continental climate
 675 during the Pleistocene: a complete astronomically tuned climatic record from Lake Baikal, SE Siberia.
 676 *Quaternary Science Reviews* 25, 3431–3457. <https://doi.org/10.1016/j.quascirev.2006.10.002>.
- 677 Sabatino, N., Ferraro, S., Coccioni, R., Bonsignore, M., Del, M., Tancredi, V., et al. 2018. Mercury anomalies in
 678 upper Aptian-lower Albian sediments from the Tethys realm. *Palaeogeography, Palaeoclimatology,*
 679 *Palaeoecology* 495, 163–170. <https://doi.org/10.1016/j.palaeo.2018.01.008>.
- 680 Selby, D., Mutterlose, J., and Condon, D.J., 2009. U-Pb and Re-Os Geochronology of the Aptian/Albian and
 681 Cenomanian/Turonian stage boundaries: implications for timescale calibration, osmium isotope seawater
 682 composition and Re-Os systematics in organic-rich sediments. *Chemical Geology* 265, 394–409.
 683 <https://doi.org/10.1016/j.chemgeo.2009.05.005>.
- 684 Thomson, D. J. 1982., Spectrum estimation and harmonic analysis, *P. IEEE* 70, 1055–1096. <https://doi.org/10.1109/9.921982>
 685 9219/82/0900-1055.
- 686 Thomson, D. J., 1990., Quadratic-Inverse Spectrum Estimates: Applications to Palaeoclimatology, *Philos. T. R.*
 687 *Soc. Lond. A.*, 332, 539–597. <https://doi.org/10.1098/rsta.1990.0130>.
- 688 Wagner, T., Herrle, J.O., Sinninghe Damsté, J.S., Schouten, S., Stüsser, I., Hofmann, P., 2008. Rapid warming
 689 and salinity changes of Cretaceous surface waters in the subtropical North Atlantic. *Geology* 36, 203–
 690 206. <https://doi.org/10.1130/G24523A.1>.
- 691 Wang, Y., Bodin, S., Blusztajn, J.S., Ullmann, C., and Nielsen, S.G., 2022, Orbitally paced global oceanic
 692 deoxygenation decoupled from volcanic CO₂ emission during the middle Cretaceous Oceanic Anoxic
 693 Event 1b (Aptian-Albian transition): *Geology*, 50, 1324–1328. <https://doi.org/10.1130/G50553.1>.
- 694 Wilpshaar, M., Leereveld, H., 1994. Palaeoenvironmental change in the Early Cretaceous Vocontian Basin (SE
 695 France) reflected by dinoflagellate cysts. *Review of Palaeobotany and Palynology* 84, 121-128.
 696 [https://doi.org/10.1016/0034-6667\(94\)90046-9](https://doi.org/10.1016/0034-6667(94)90046-9).
- 697 Zhang, Y., Ogg, J.G., Mínguez, D., Hounslow, M.W., Olausson, S., Gradstein, F. M., Esmeray-Senlet, S., 2021.
 698 Magnetostratigraphy of U-Pb–dated boreholes in Svalbard, Norway, implies that magnetochron M0r (a
 699 proposed Barremian–Aptian boundary marker) begins at 121.2 ± 0.4 Ma. *Geology* 49, 733–737.
 700 <https://doi.org/10.1130/G48591.1>.

702 **Figures captions:**

703 **Fig. 1.** Location, paleogeography, and pictures of the Col de Pré-Guittard section. A. Location
704 of the Col de Pré-Guittard section within the Vocontian Basin (from Friès and Parize 2003). B.
705 Palaeogeography of the Central-North Atlantic during the Aptian with the location of the
706 Vocontian Basin (Barrier et al. 2018). C. Overview of Col de Pré-Guittard 2 (CPG2). D. Close-
707 up view of the Paquier Level.

708 **Fig. 2.** Detailed location of the two sections of Col Pré-Guittard (CPG). A. Simplified
709 Geographic map of Col de Pré-Guittard region showing the two studied sections, the map
710 provided from the Institut Géographique National (France) available at infoterre.brgm.fr. The
711 brown circles indicate the locations of the sections and the black rectangle corresponds to the
712 area shown in (B). B. Aerial photography of the Col de Pré-Guittard, area available at
713 <https://www.geoportail.gouv.fr/>.

714 **Fig. 3.** Long-term evolution of geochemical proxies along the CPG-1 and CPG-2. A.
715 Stratigraphic evolution of the Magnetic susceptibility (MS, $\times 10^{-8} \text{ m}^3 \cdot \text{kg}^{-1}$) records from the
716 CPG-1. B. Magnetic susceptibility (MS, $\times 10^{-8} \text{ m}^3/\text{kg}$) records from the CPG-2. From C to F.
717 Trend evolution of total organic carbon (TOC, wt.%), hydrogen index (HI, mgHC/g TOC),
718 oxygen index (OI, mgCO₂/g TOC) and $\delta^{13}\text{C}_{\text{org}}$ (‰ VPDB) records respectively from CPG-2.
719 The light brown color defines the position of the four events (Jacob, Kilian, Paquier and
720 Leenhardt) and the red line corresponds to the long-term trend of the series in different proxies.

721 **Fig. 4.** Cross plots of the magnetic susceptibility vs carbonate contents for CPG-2. The red line
722 represents the linear regression with the correlation coefficients.

723 **Fig.5:** Stratigraphic evolution of TOC, HI and $\delta^{13}\text{C}_{\text{org}}$ along Col de Pré Guittard (this study)
724 compared to Les Briers section, data are from Bodin et al. (2023).

725

726 **Fig. 6.** 2π Multi-Taper Method (MTM) spectra with Coefficient Correlation COCO analysis for
727 CPG-1. Periods are labelled in meters in the spectral peaks and labeled with different colors,
728 red for 405-kyr eccentricity, orange for 100-kyr eccentricity, and green for obliquity and blue
729 for 20-kyr precession.

730 **Fig. 7.** Spectral analyses and astrochronology of the CPG-1. A. Raw MS signal. B. Filters of
731 the 405-kyr band (red color) and the 100-kyr band (orange color). C. Amplitude spectrograms
732 performed on 25-m width windows. D. Amplitude spectrograms performed on 10-m width
733 windows after filtering the lowest frequencies. E. H_0 significance levels at sedimentation rates
734 ranging from 0.7 to 6 cm/kyr calculated with the eCOCO procedure performed on 25-m width
735 windows.

736 **Fig. 8.** 2π Multi-Taper Method (MTM) with Coefficient Correlation COCO analysis for the
737 CPG2. Periods are labelled in meters with different colors, red for 405-kyr eccentricity, orange
738 for 100-kyr eccentricity, and green for obliquity and blue for 20-kyr precession.

739 **Fig. 9.** Spectral analyses of CPG-2. A. Raw MS signal. B. Filters of the 405-kyr band (red color)
740 and the 100-kyr band (orange color). C. Amplitude spectrograms performed on 40-m width
741 windows. D. Amplitude spectrograms performed on 15-m width windows. E. H_0 significance
742 level at sedimentation rates ranging from 0.7 to 10 cm/kyr calculated with the eCOCO
743 procedure performed on 40-m width windows

744 **Fig.10:** Revised spectral analysis was conducted on the Col de Pré Guittard section using data
745 provided by Charbonnier et al. (2023). A. Raw magnetic susceptibility data is represented in
746 black, while the long-term evolution is shown in red. B and C displays spectrograms with
747 windows sizes of 60 m and 15 m, respectively. The significant periods are labeled in meters. D
748 and E demonstrate the H_0 significance level calculated from eCOCO analysis, performed on
749 width windows at 60 m and 25 m, respectively, indicating the mean average sedimentation rate.

750 F, G, and H present the 2π -Multi-Taper Method (MTM) spectra conducted on three subdivided
751 intervals: interval 1 (from the base of the series to 320 m), interval 2 (from 315 m to 365 m),
752 and finally, interval 3 (from 360 m to the top of the series).

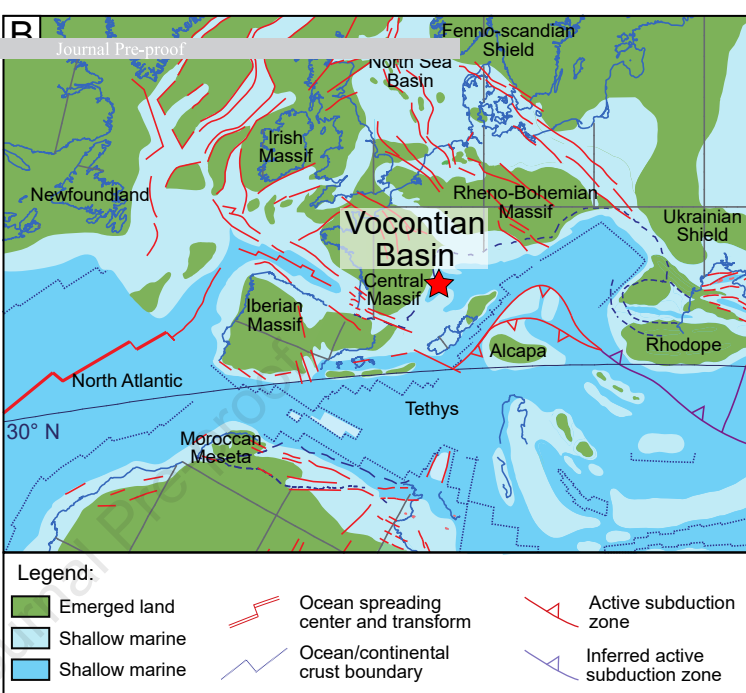
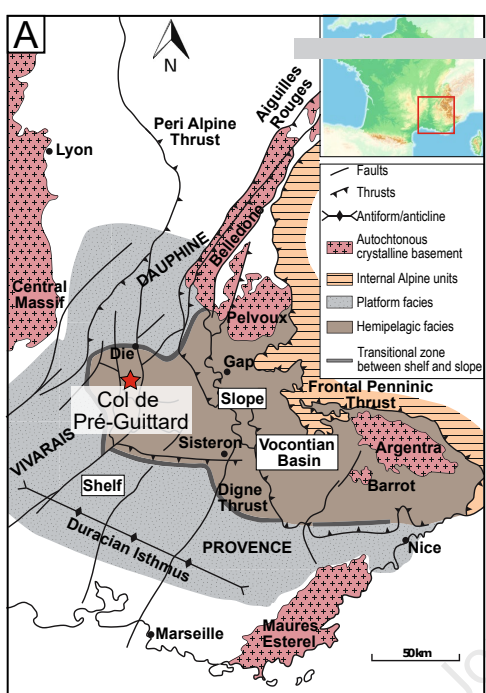
753 **Fig. 11.** An overview of the astronomical calibration of Col de Pré Guittard section (CPG 2)
754 correlated to the recent data provided from les Briers section, CaCO_3 data are from Bodin et al.
755 (2023). A. Raw MS signal. B. Filters of the 405-kyr band (red color) and the 100-kyr band
756 (orange color) C. Raw CaCO_3 while the long-term evolution is shown in red. D. Filter of the
757 405-kyr band (red color).

758 **Fig. 12.** 2π Multi-Taper Method (MTM) analysis performed on CaCO_3 carbonate content from
759 Les Briers section, data provided from Bodin et al. (2023).

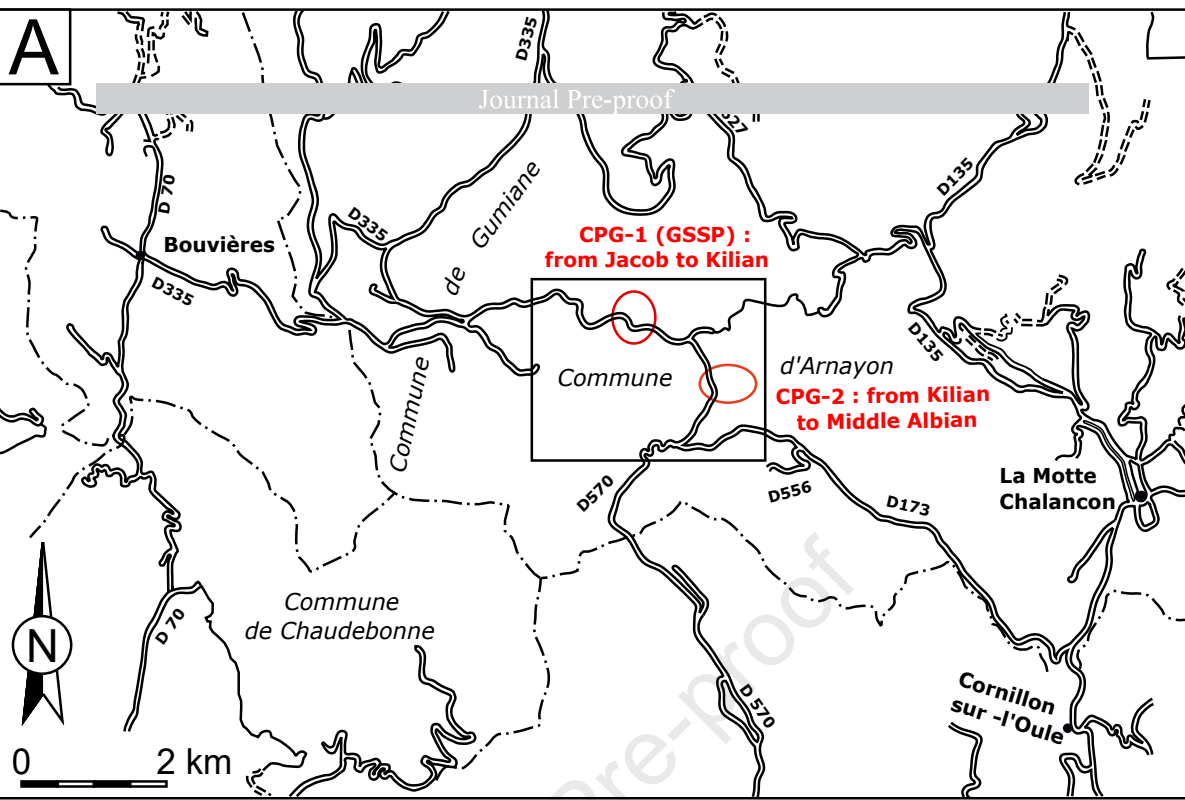
760 **Fig. 13.** Correlations of astronomical time scale for the Jacob-Kilian interval in Piobbico core,
761 Central Italy (Huang et al. 2010) and Col de Pré-Guittard section, Vocontian basin (present
762 study), and Poggio le Guanine core (Leandro et al. 2022).

763

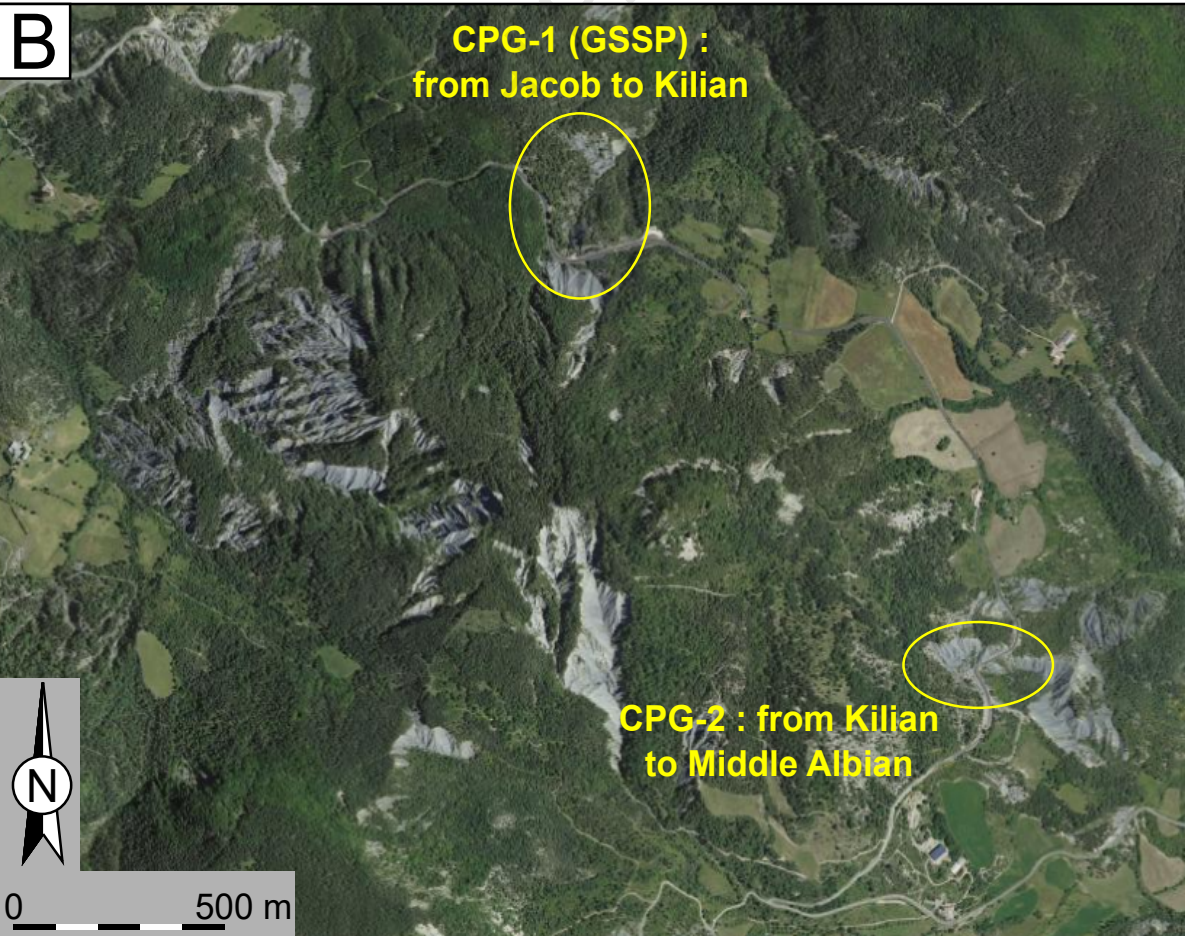
764

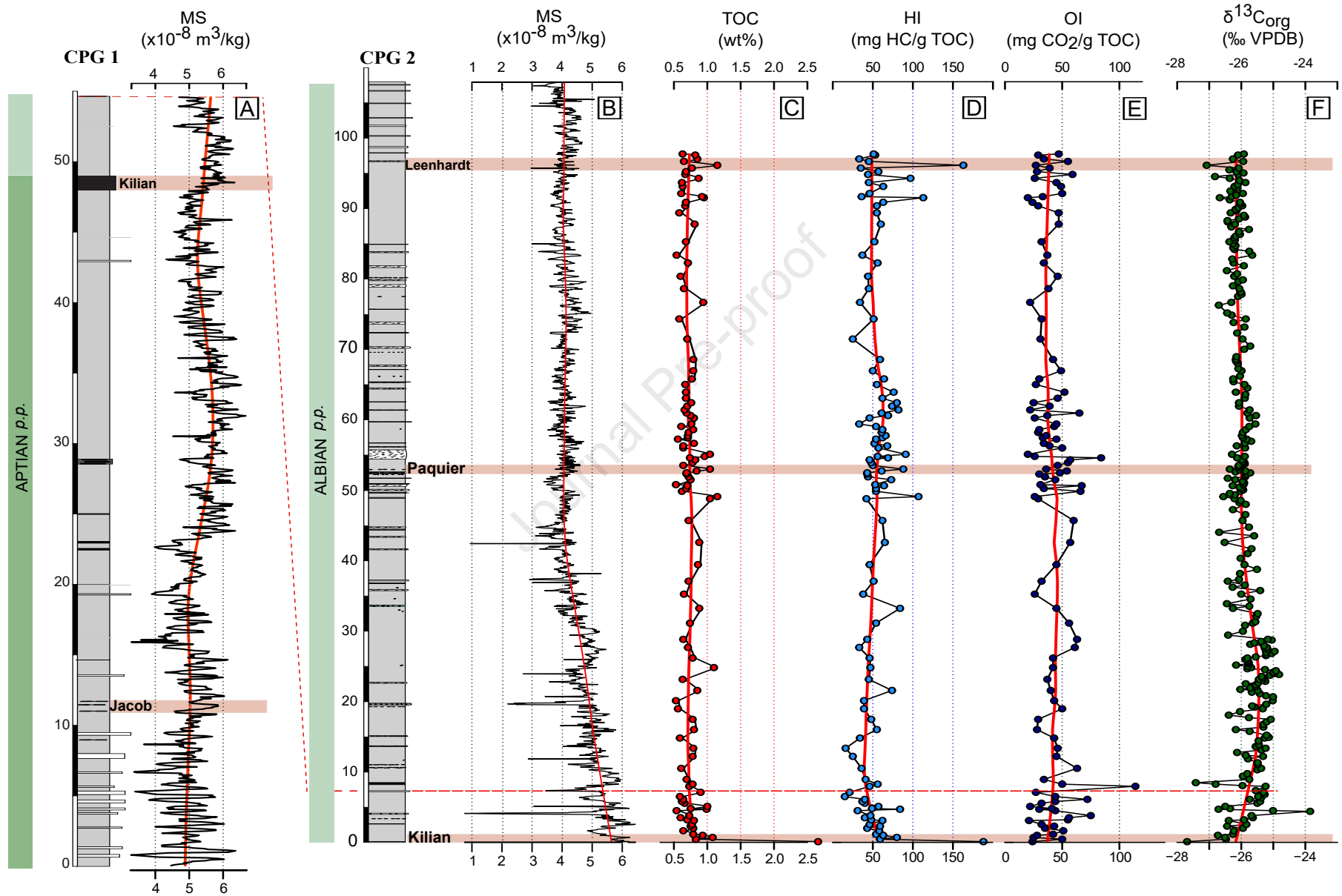


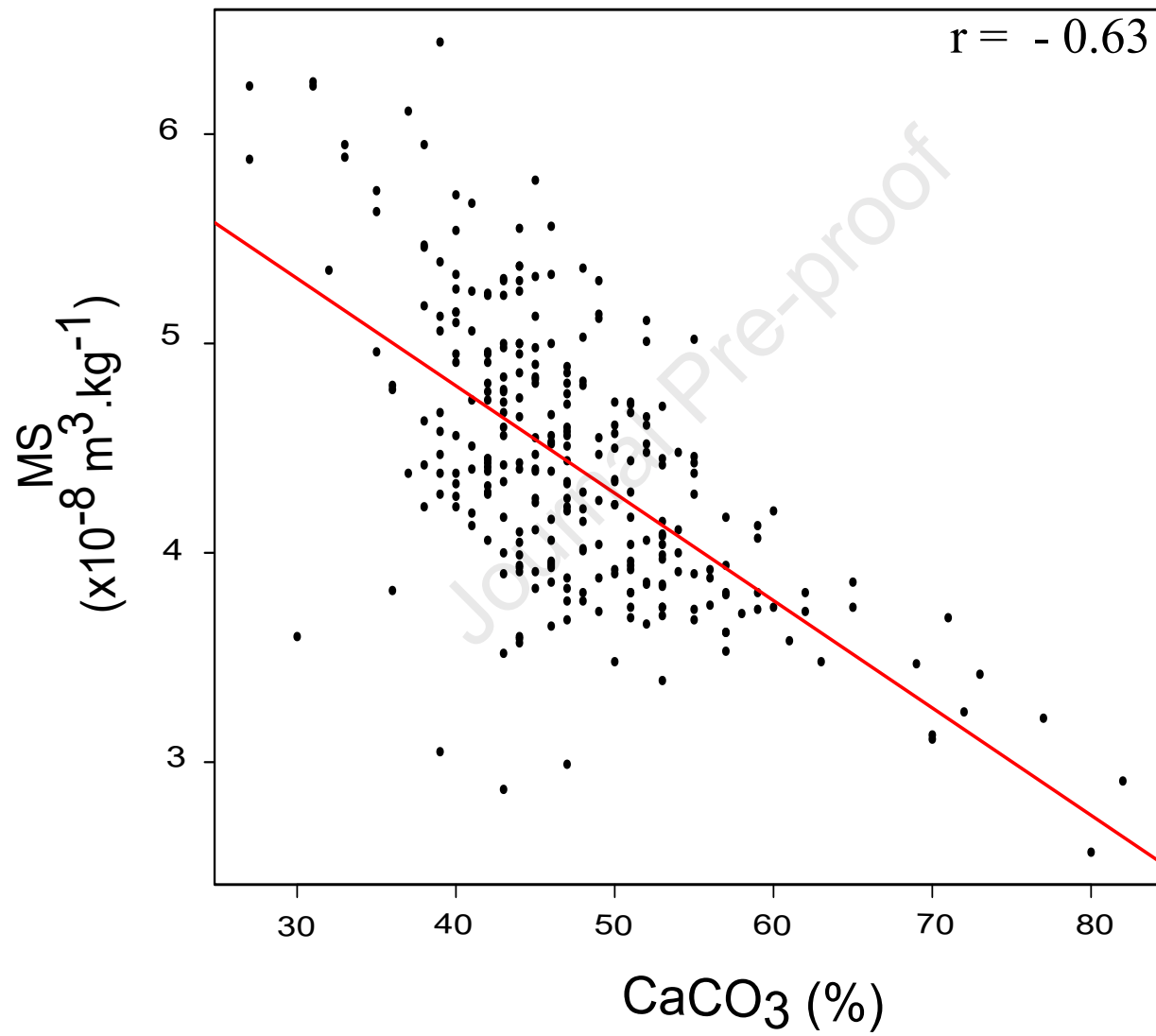
A

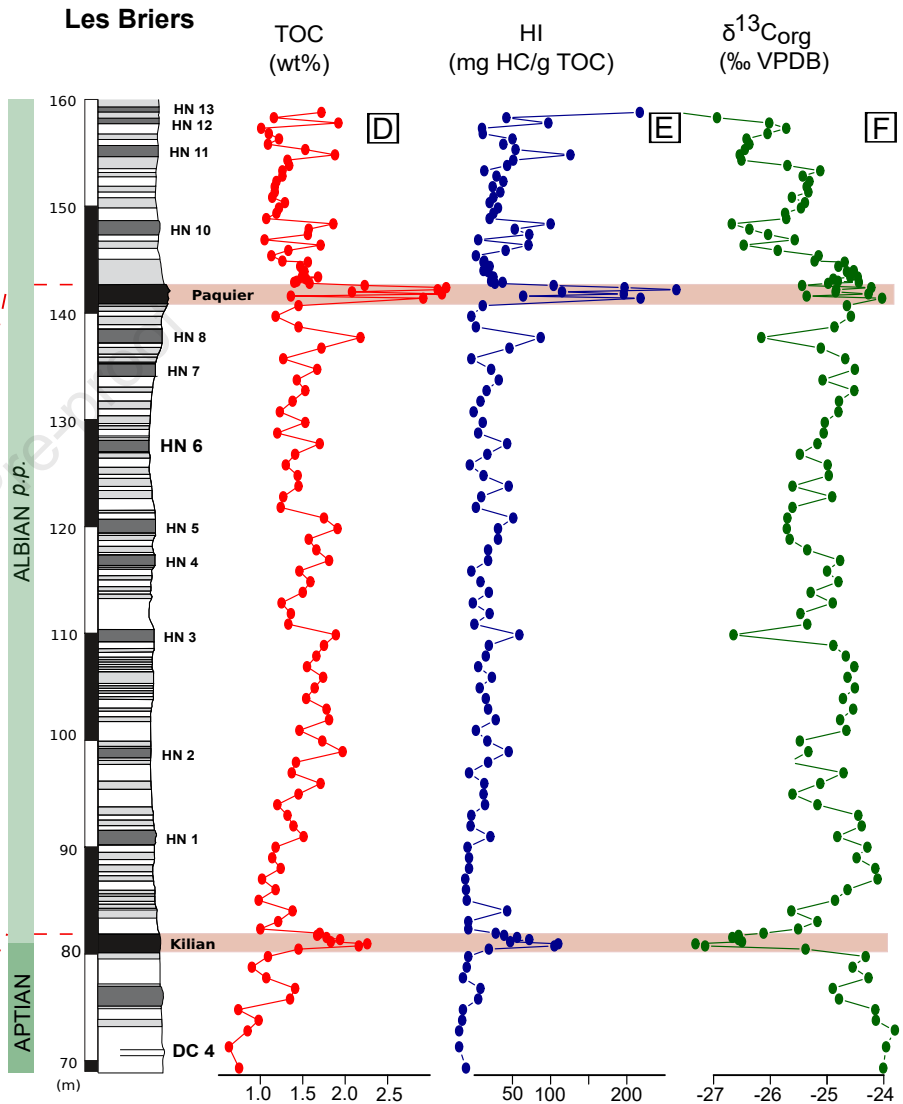
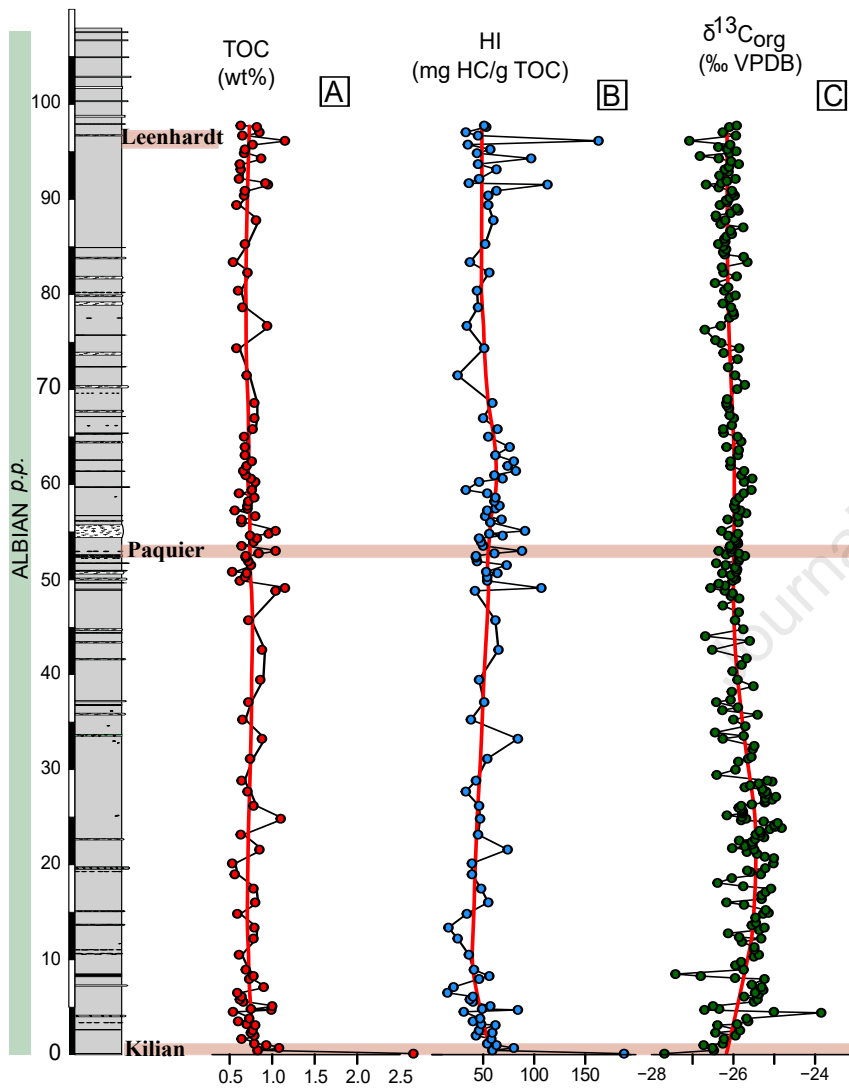


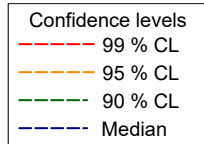
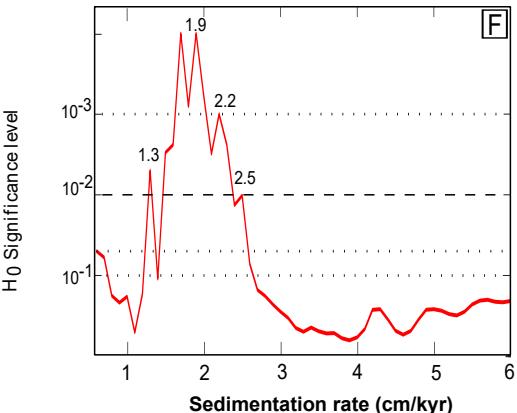
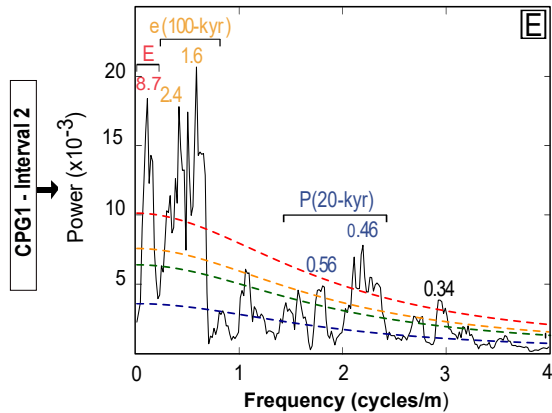
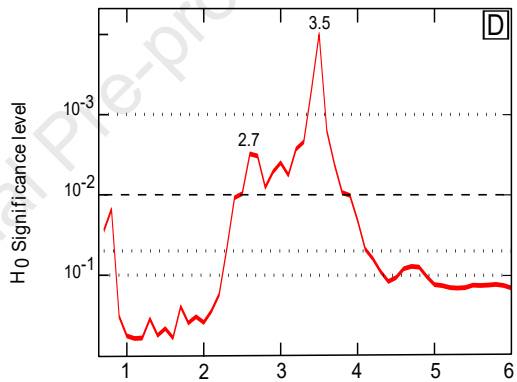
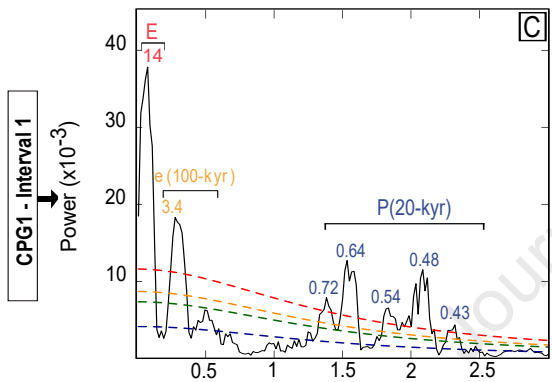
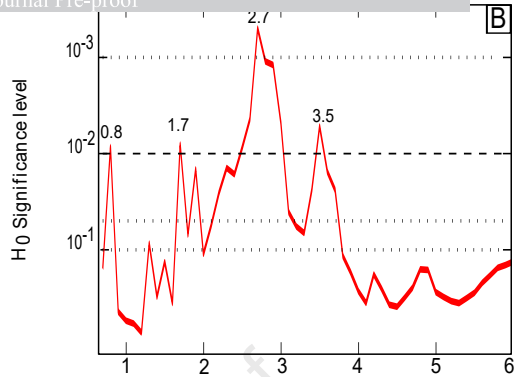
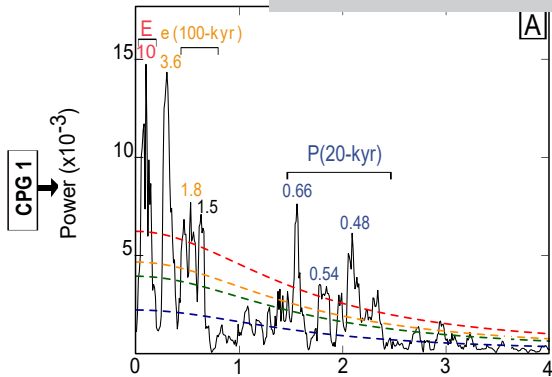
B

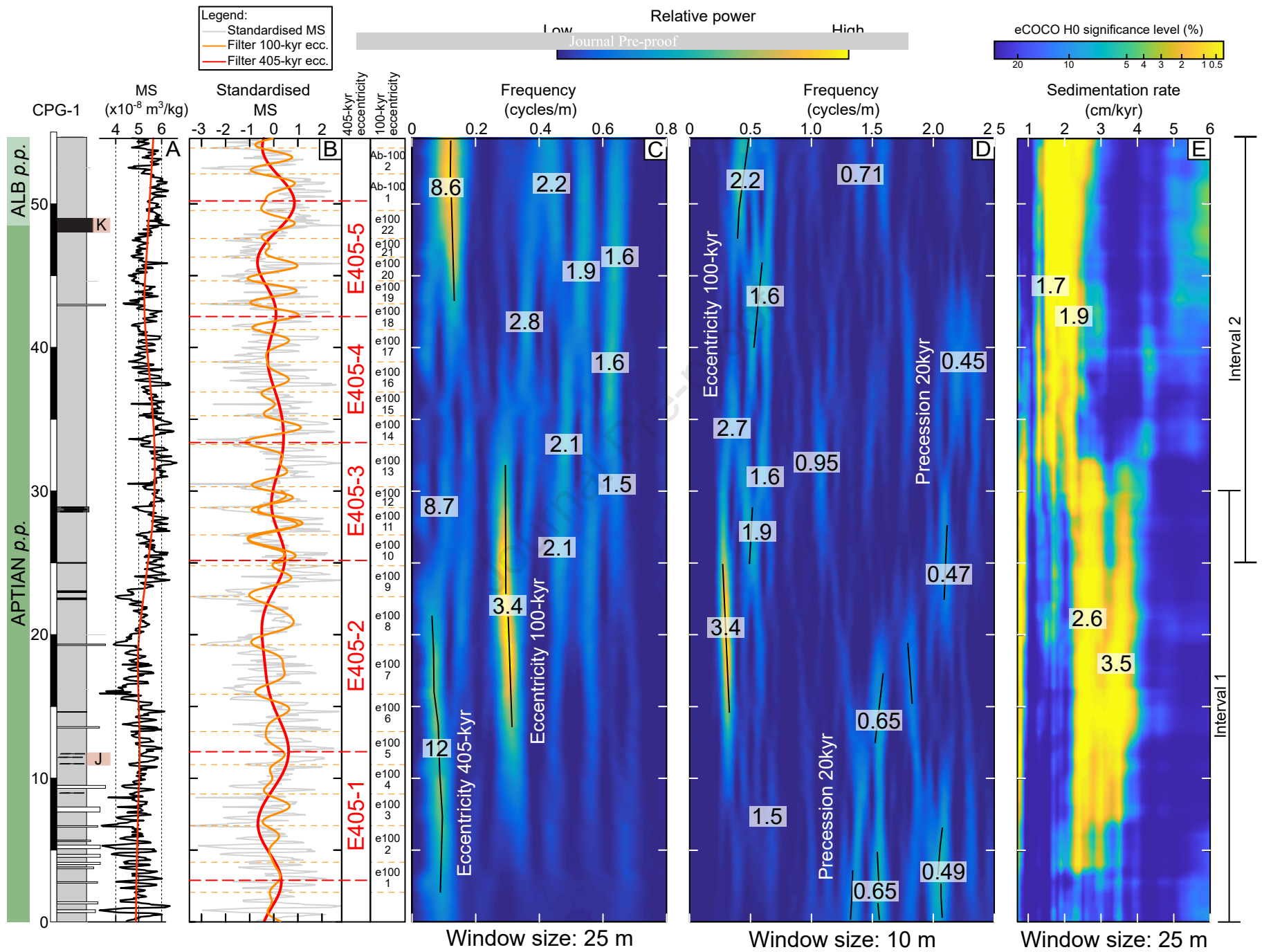


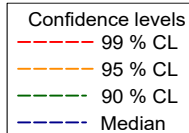
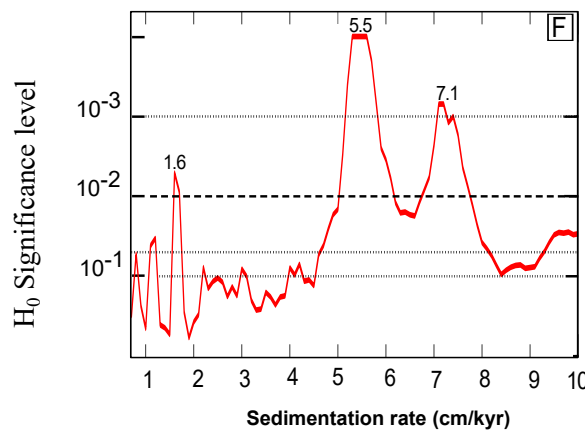
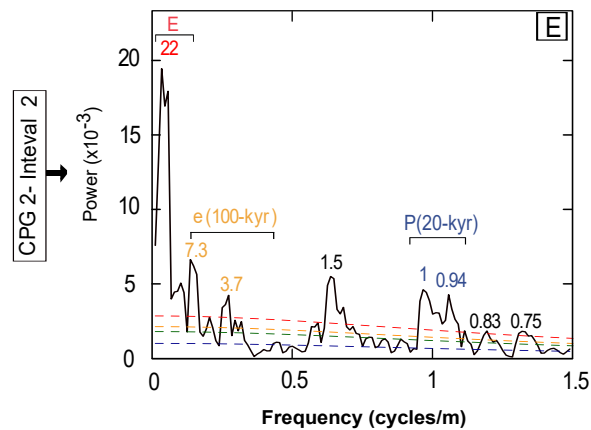
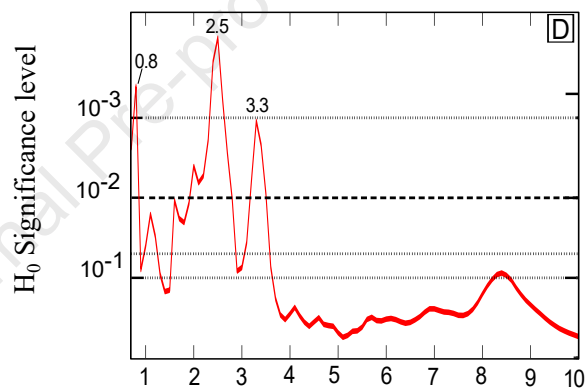
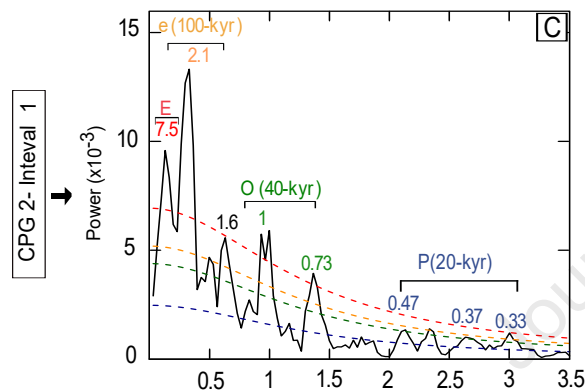
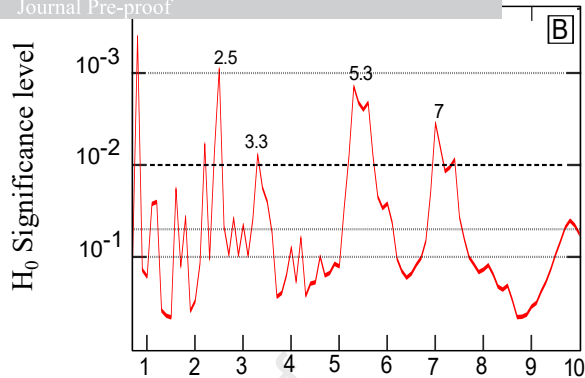
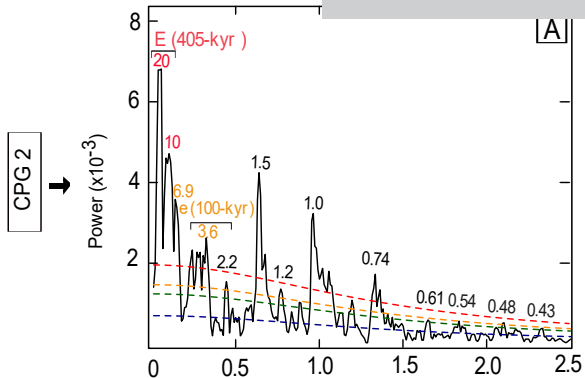


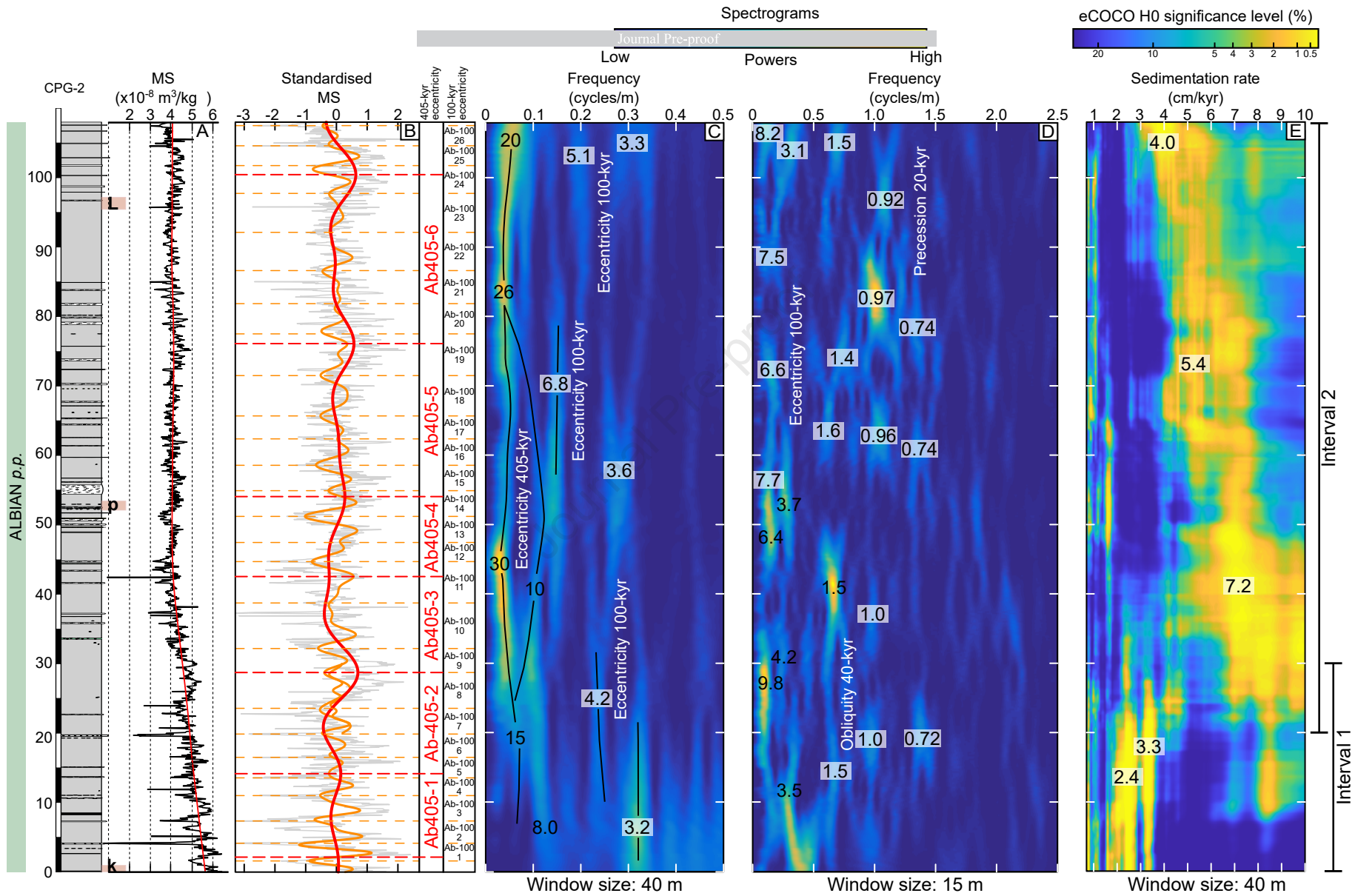


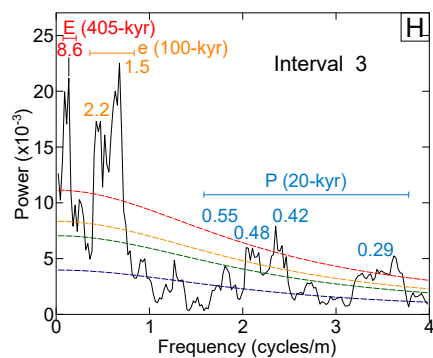
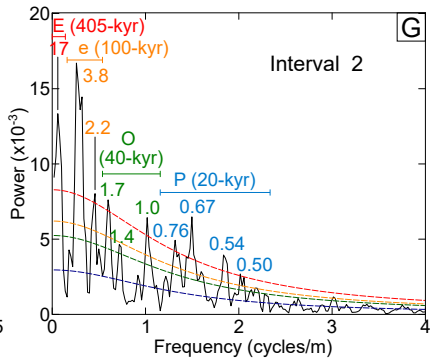
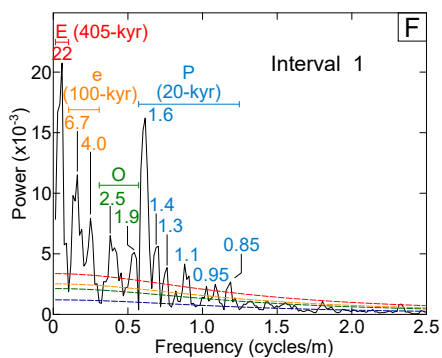
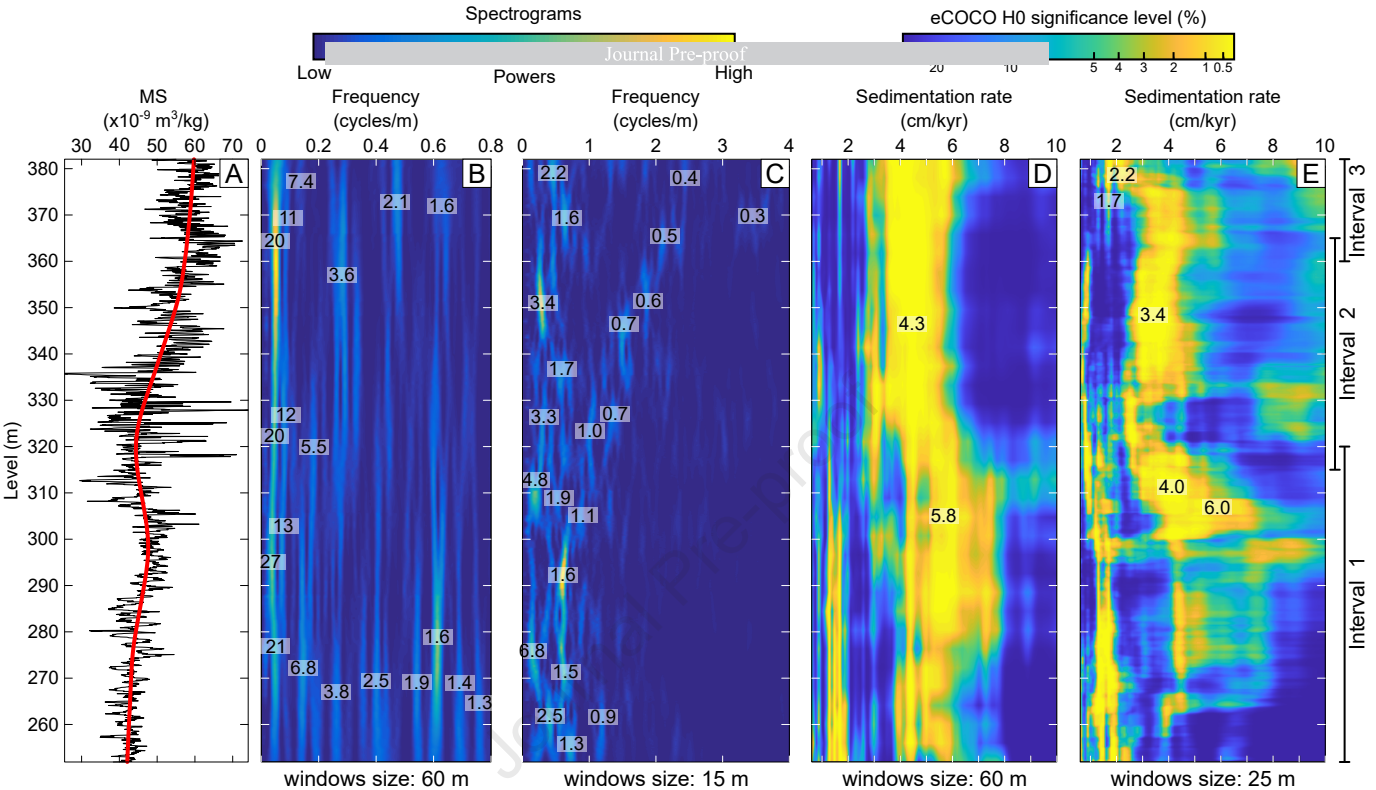






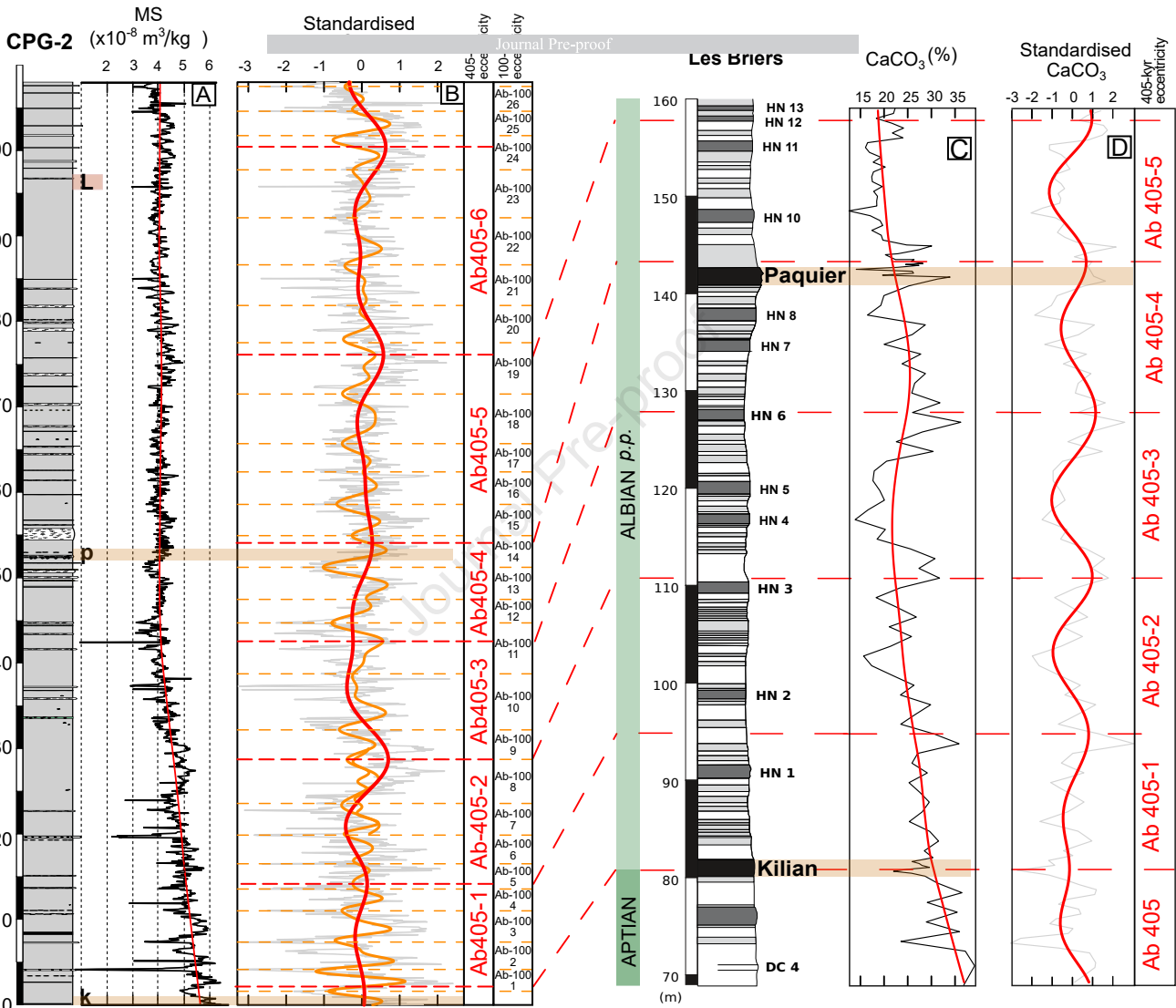


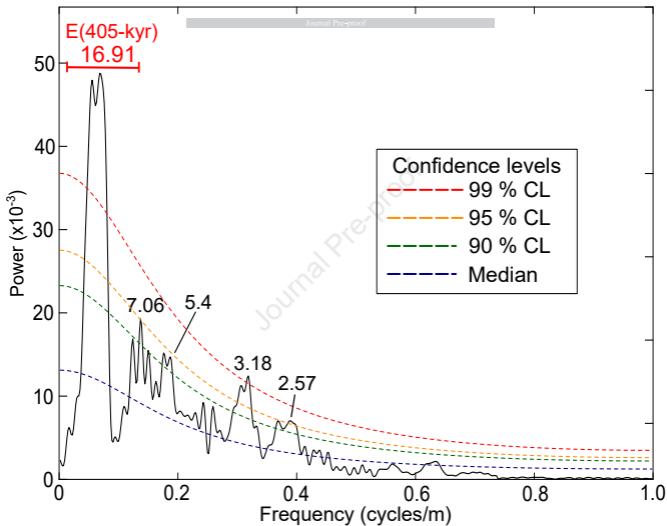


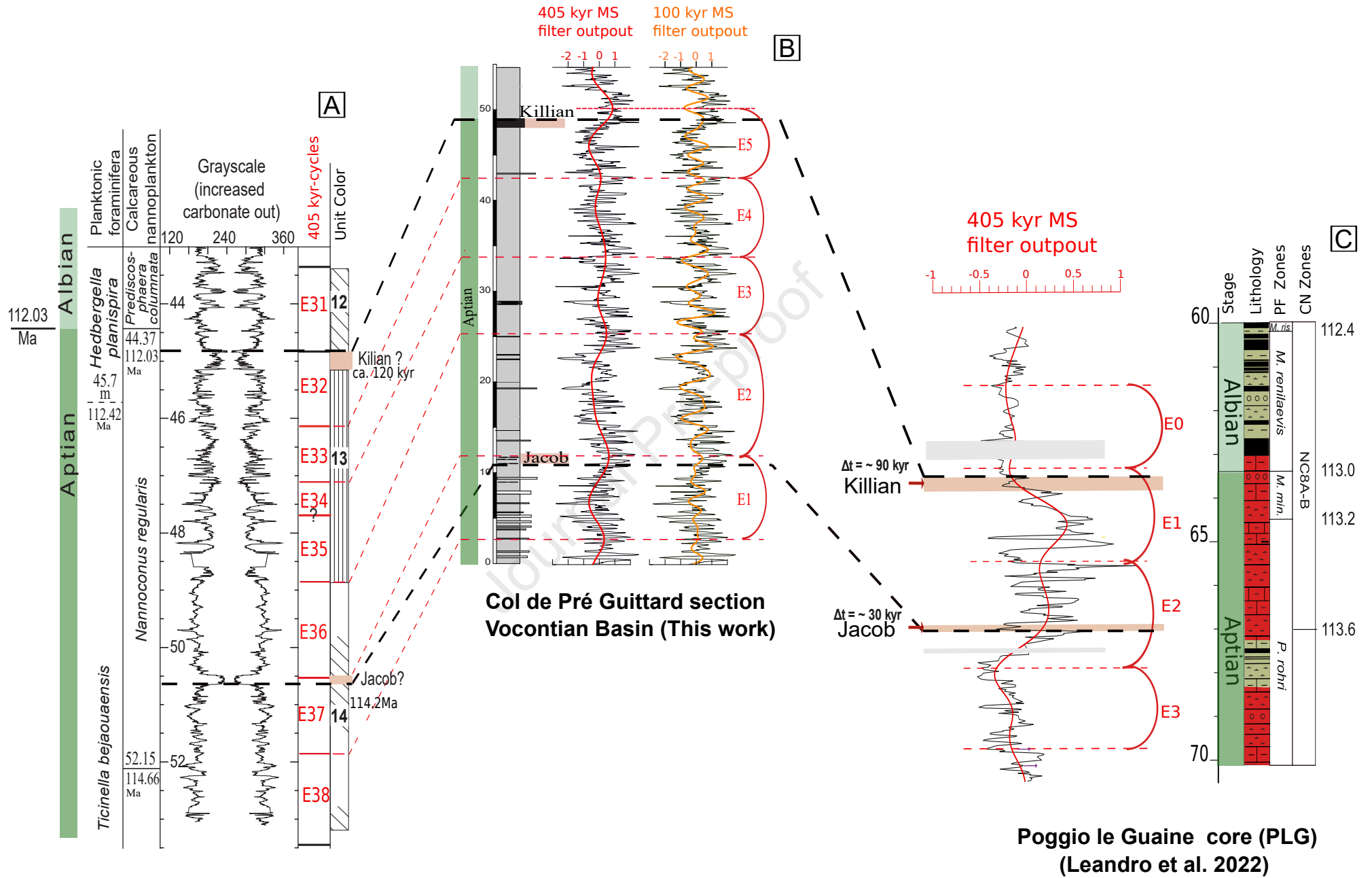


Confidence levels









Piobbico core
Central Italy
(Huang et al. 2010)

Poggio le Guaine core (PLG)
(Leandro et al. 2022)

Highlights

- Astronomical calibration of the OAE 1b interval in Col de Pré-Guittard section, GSSP of the Albian.
- Jacob, Kilian, Paquier and Leenhardt events located near maximums of the 405-kyr eccentricity cycle in magnetic susceptibility
- Concomitant impact of 405-kyr eccentricity and volcanism on the onset of these events

Journal Pre-proof

Declaration of interests

The authors declare that they have no known competing financial interests or personal relationships that could have appeared to influence the work reported in this paper.

The authors declare the following financial interests/personal relationships which may be considered as potential competing interests:

Ait-Itto Fatima-Zahra reports financial support was provided by Make our planet great again (MOPGA). Mathieu Martinez reports financial support was provided by National Centre for Scientific Research MITI Le Temps AstroCarb. AIT-ITTO Fatima-Zahra reports financial support was provided by project SAD METOX from Région Bretagne. Mathieu Martinez reports financial support was provided by Défis Scientifiques program from Université de Rennes.